Kinematics of polygonal fault systems: observations from the northern North Sea

Thilo Wrona[1*], Christopher A. Jackson[2], Craig Magee[2], Mads Huuse[3], Kevin G. Taylor[3]

[1]Department of Earth Science, University of Bergen, Norway, [2]Department of Earth Science and Engineering, Imperial College London, United Kingdom, [3]School of Earth and Environmental Sciences, University of Manchester, United Kingdom

Submitted to Journal:
Frontiers in Earth Science

Specialty Section:
Structural Geology and Tectonics

Article type:
Original Research Article

Manuscript ID:
305423

Received on:
05 Sep 2017

Revised on:
04 Nov 2017

Frontiers website link:
www.frontiersin.org

Conflict of interest statement

The authors declare that the research was conducted in the absence of any commercial or financial relationships that could be construed as a potential conflict of interest

Author contribution statement

This research was part of the PhD project of TW. The research plan was thus developed between the PhD candidate (TW), the supervisors (CALJ, MH, KGT) and a colleague (CM). The seismic data used in this study was acquired by Norsk Hydro AS in 1992 and subsequently made publicly available, together with the well data, by the Norwegian Petroleum Directorate. The data analysis and interpretation was conducted by all authors. The manuscript was also developed, written and revised by all authors. All authors approved the final version of the manuscript and thus agree to be accountable for this work.

Keywords

Polygonal faults, normal faults, Fine-Grained Sediments, Mudstones, shale, Diagnesis, opal-A, Opal-CT, compaction, Dewatering, Fluid flow, Sediment remobilization, rock mechanics

Abstract

Word count: 219

Layer-bound, low-displacement normal faults, arranged into a broadly polygonal pattern, are common in many sedimentary basins. Despite having constrained their gross geometry, we have a relatively poor understanding of the processes controlling the nucleation and growth (i.e. the kinematics) of polygonal fault systems. In this study we use high-resolution 3-D seismic reflection and borehole data from the northern North Sea to undertake a detailed kinematic analysis of faults forming part of a seismically well-imaged polygonal fault system hosted within the up to 1000 m thick, Early Palaeocene-to-Middle Miocene mudstones of the Hordaland Group. Growth strata and displacement-depth profiles indicate faulting commenced during the Eocene to early Oligocene, with reactivation possibly occurring in the late Oligocene to middle Miocene. Mapping the position of displacement maxima on 137 polygonal faults suggests that the majority (64%) nucleated in the lower 500 m of the Hordaland Group. The uniform distribution of polygonal fault strikes in the area indicates that nucleation and growth were not driven by gravity or far-field tectonic extension as has previously been suggested. Instead, fault growth was likely facilitated by low coefficients of residual friction on existing slip surfaces, and probably involved significant layer-parallel contraction (strains of 0.01-0.19) of the host strata. To summarize, our kinematic analysis provides new insights into the spatial and temporal evolution of polygonal fault systems.

Funding statement

We would like to thank the Department of Earth Science and Engineering, Imperial College for the Janet Watson scholarship that made this research possible.

Ethics statements

(Authors are required to state the ethical considerations of their study in the manuscript, including for cases where the study was exempt from ethical approval procedures)

Does the study presented in the manuscript involve human or animal subjects: No

Title: Kinematics of polygonal fault systems: observations from the northern North Sea

Authors: Thilo Wrona[1,2]*, Craig Magee[1], Christopher A-L. Jackson[1], Mads Huuse[3] and Kevin G. Taylor[3]

[1]*Basins Research Group (BRG), Department of Earth Science and Engineering, Imperial College, Prince Consort Road, London, SW7 2BP, UK*

[2]*Now at: Department of Earth Science, University of Bergen, Allégaten 41, N-5007 Bergen, Norway*

[3]*School of Earth and Environmental Sciences, University of Manchester, Williamson Building, Oxford Road, Manchester M13 9PL, UK*

*Corresponding author (thilo.wrona@uib.no)

ABSTRACT:

Layer-bound, low-displacement normal faults, arranged into a broadly polygonal pattern, are common in many sedimentary basins. Despite having constrained their gross geometry, we have a relatively poor understanding of the processes controlling the nucleation and growth (i.e. the kinematics) of polygonal fault systems. In this study we use high-resolution 3-D seismic reflection and borehole data from the northern North Sea to undertake a detailed kinematic analysis of faults forming part of a seismically well-imaged polygonal fault system hosted within the up to 1000 m thick, Early Palaeocene-to-Middle Miocene mudstones of the Hordaland Group. Growth strata and displacement-depth profiles indicate faulting

commenced during the Eocene to early Oligocene, with reactivation possibly occurring in the late Oligocene to middle Miocene. Mapping the position of displacement maxima on 137 polygonal faults suggests that the majority (64%) nucleated in the lower 500 m of the Hordaland Group. The uniform distribution of polygonal fault strikes in the area indicates that nucleation and growth were not driven by gravity or far-field tectonic extension as has previously been suggested. Instead, fault growth was likely facilitated by low coefficients of residual friction on existing slip surfaces, and probably involved significant layer-parallel contraction (strains of 0.01-0.19) of the host strata. To summarize, our kinematic analysis provides new insights into the spatial and temporal evolution of polygonal fault systems.

1. INTRODUCTION

Polygonal fault systems have been documented in over 100 basins worldwide and comprise large numbers of layer-bound, low-displacement (<100 m throw), normal faults, which in plan-view have a polygonal arrangement and cover areas of up to 2,000,000 km^2 (Fig. 1 and review by Cartwright 2011). These polygonal fault systems occur within fine-grained sedimentary successions, which commonly form seals for hydrocarbon reservoirs (e.g. Cartwright et al. 2007; Jackson et al. 2014), CO_2 storage sites (e.g. Arts et al. 2004), and nuclear waste disposal sites (e.g. Dehandschutter et al. 2005a). Because polygonal fault systems have the potential to reduce or enhance the sealing capacity of such fine-grained sedimentary successions (e.g. Gay and Berndt 2007; Huuse et al. 2010), it is critical to understand their kinematics.

In general, polygonal faulting appears linked to dewatering and compaction of fine-grained sediments (e.g. Cartwright et al. 2003), although the exact driving mechanism(s) remain(s) unclear. Several mechanisms have been proposed including: (1) density inversion by differential compaction between the host succession and the overlying strata (Henriet et al.

1988; Watterson et al. 2000); (2) internal layer-parallel extension of the host succession driven by gravitational sliding (Higgs and McClay 1993; Clausen et al. 1999); (3) hydraulic fracturing due to differential compaction and overpressure build-up (Cartwright 1994b, a); (4) syneresis (i.e. spontaneous contraction of a sediment-water gel (Dewhurst et al. 1999); (5) low coefficients of residual friction that are too low to sustain *in situ* stresses along the fault plane (Goulty 2001, 2002, 2008); (6) particle dissolution during diagenesis, which induces tensile stresses of sufficient magnitude for normal faulting (Shin et al. 2008; Cartwright 2011); and (7) yielding, which describes behaviour of clays not captured by classic Mohr-Coulomb or Drucker-Prager criteria (Laurent et al. 2012). There is thus clearly a lack of consensus on the mechanism driving polygonal faulting, reflecting, at least in part, our poor understanding of their kinematics.

This study examines the kinematics of a polygonal fault system developed in the Cenozoic succession of the northern North Sea. The area of interest covers ~740 km^2 and contains >1500 faults, forming part of a significantly larger, basin-scale system (Cartwright and Lonergan 1996). Due to the availability of comprehensive lithological and mineralogical data, and high-quality 3-D seismic reflection data, the northern North Sea provides an ideal natural laboratory to study the geometry and kinematics of polygonal fault systems. We extract detailed stratigraphic thickness variations throughout the host succession to constrain the timing of faulting and map the geometry and displacement distributions of 137 polygonal faults in this system. This approach allows us to constraining polygonal fault kinematics, including their nucleation sites and growth history. Finally, we obtain accurate 1-D and 2-D strain estimates to investigate the effect of this fault system on the compaction of the host strata.

2. GEOLOGICAL SETTING

The North Viking Graben formed during the Middle Jurassic to Early/Middle Cretaceous in response to crustal extension (Fig. 2). Jurassic rifting was characterised by rapid tectonic subsidence and formation of large-displacement normal faults that bounded graben and half-graben (Badley et al. 1988; Yielding 1990; Faerseth et al. 1997). The post-rift sag phase began in the Early Cretaceous, marking the transition from fault- to thermally-controlled subsidence (Joy 1993; Jordt et al. 2000; Kyrkjebø et al. 2001; Faleide et al. 2002). Subsequently, the North Viking Graben has undergone two major uplift events: (1) an early Palaeocene phase related to rifting, magmatism, and the break-up of the NE Atlantic (e.g. Nadin and Kusznir 1995); and (2) a middle Miocene phase, possibly related to long-wavelength doming during regional compression (e.g. Løseth et al. 2013).

During the sag phase, the North Viking Graben was filled by sediment derived from the uplifted basin margins, with up to 5 km of predominantly fine- to very fine-grained, marine mudstones deposited (i.e. Shetland, Rogaland, Hordaland and Nordland groups; Fig. 2d) (Rundberg 1989; Jordt et al. 2000; Anell et al. 2012). This study focusses on a regionally-extensive polygonal fault system hosted within the Early Palaeocene-to-Middle Miocene Hordaland Group. The Hordaland Group is underlain by the Balder Formation (Rogaland Group), which primarily consists of poorly-consolidated mudstone and volcanic tuff (Knox and Holloway 1992; Graham et al. 2003). The top of the Hordaland Group and the polygonally faulted succession is marked by the mid-Miocene unconformity, a regional unconformity formed by non-deposition and erosion that spans approximately 10 Ma (e.g. Eidvin and Rundberg 2001; Løseth et al. 2013). This erosional event was followed in the Late Miocene to Early Pliocene by deposition of the sandy Utsira Formation and, during the Pliocene and Pleistocene, by marine mudstones of the Nordland Group (e.g. Jordt et al. 1995; Rundberg and Eidvin 2005).

After deposition, the Hordaland Group, which hosts the polygonal fault system of interest, has undergone the first stage of silica diagenesis, i.e. the transformation of amorphous, biogenic silica (opal-A) to cristobalite/tridymite lepispheres (opal-CT), which changed the density and acoustic properties of the host sequence, thereby giving rise to a discrete, mappable seismic reflection (Wrona et al. 2017a; Wrona et al. 2017b). The co-existence of silica diagenesis and polygonal fault systems in other basins (Davies et al. 2006) has led some authors to suggest a genetic link between polygonal faulting and diagenesis (Shin et al. 2008; Davies et al. 2009; Cartwright 2011; Davies and Ireland 2011). It is thus worth noting that the transformation from opal-A to opal-CT probably migrated upward through the lower Hordaland Group, initiating in the Middle or Late Eocene and continuing, potentially, to the present (Wrona et al. 2017a). Apart from the opal-A/CT transformation, the Hordaland Group shows no other significant compositional and diagenetic changes affecting physical rock properties (Wrona et al. 2017b).

3. DATA

3.1 Well data

This study uses well data from exploration well 35/10-1 and 35/11-5, which constrain the age, composition, and diagenetic state of the Hordaland Group mudstones in the North Viking Graben (Wrona et al. 2017a). Moreover, we use checkshot data from exploration well 31/2-8 to convert a sub-volume of the 3-D seismic volume from time- to depth domain (Fig. S1). For the depth conversion, we defined four intervals: (1) water column; (2) Nordland Group; (3) Hordaland Group (i.e. the interval containing the polygonal fault system); and (4) sub-Hordaland Group strata. We derive best-fit linear velocity-depth functions for each interval using checkshot data of exploration well 31/2-8, converting two-way traveltimes (milliseconds) to depths (metres) (Fig. S1).

3.2 3-D seismic data

We use a 3-D seismic volume (MN9201_R05) volume covering an area of ~1440 km^2 (Fig. 2a, b). The data were recorded using a series of 3600 m long streamers with 144 groups. This setup results in a nominal 36-fold coverage with a line spacing of 25 m. These multi-channel data were recorded with a vertical sampling of 4 ms. The seismic volume is time-migrated and zero-phase processed with SEG reverse polarity; i.e. an acoustic impedance increase with depth is represented by a negative reflection event (black), and a decrease in acoustic impedance with depth is represented by a positive reflection event (white) (e.g. Fig. 2d).

Vertical seismic resolution describes the ability to image a geological feature (e.g. a bed or fault) and is, to a first degree, a function of the dominant frequency and seismic velocity in the interval of interest (Brown 2004). Seismic resolution can be defined as *the limit of separability*, i.e. the thickness below which reflections from two successive interfaces start to interfere and appear as a tuned reflection package, and the *limit of visibility*, i.e. the minimum thickness at which reflections from two successive interfaces can be imaged (Brown 2004). Using the dominant frequency of our seismic reflection data (50 Hz) (Fig. 2d) and the average p-wave velocity of the Hordaland Group (~2000 m s^{-1}) (Fig. S1), *the limit of separability* (i.e. a quarter of the wavelength) is ~10 m, whilst *the limit of visibility* can be as low as ~1 m (i.e. a thirtieth of the wavelength) depending on the signal-to-noise ratio of the data and the acoustic impedance contrasts at the interfaces (Brown 2004). The data are thus of sufficient quality to allow us to map fault displacements and stratigraphic thickness variations as small as 10 m.

4. METHODS

4.1 Seismic interpretation

We map seismic reflections bounding the top and base of the polygonal fault system over an area of ~740 km^2 (mid Miocene unconformity and top Balder Formation; Fig. 2d). We also map a high-amplitude seismic reflection produced by the opal-A/CT transformation (Wrona et al. 2017a), calculating the coherency attribute (*sensu* Bahorich and Farmer (1995), along this horizon to highlight the geometry and extent of the polygonal fault system (Fig. 2b). Because the polygonal fault system contains >1500 faults in the study area (Fig. 2b), we select a representative sub-volume (7.5 × 6.2 × 1.8 km) in which to conduct a quantitative geometric and displacement analysis (Fig. 3). We consider the sub-volume to be representative because the polygonal faults inside and outside its extent are all bound to the Hordaland Group; display uniform distributions of fault strikes consistently, and exhibit similar planar-to-listric cross-sectional geometries (Fig. 2).

To constrain the timing of faulting, we map thickness variations in faulted host strata. In particular, we identify hanging wall wedges that expand towards bounding faults, and cross-fault thickening, i.e. thickness increases from foot- to hanging wall (e.g. McLeod et al. 2000; Childs et al. 2003; Bell et al. 2014). To reveal these detailed stratigraphic thickness variations, we map eleven horizons (including the top and base of the polygonally faulted succession) within the depth-converted sub-volume, thereby defining ten stratigraphic packages (Fig. 3), allowing to generate high-resolution structural and thickness (isopach) maps (Figs. 4, 5). The structural maps are complemented by length-weighted rose diagrams of polygonal faults developed at that particular structural level (Fig. 4). The thickness maps shown on Fig. 5 are calculated between adjacent horizons, such that Fig. 5a shows thicknesses between the horizons shown on Fig. 4a, b. Note that we chose the number of horizons so that the thickness maps depict values well above the (vertical) seismic resolution, i.e. *the limit of separability (~10 m).*

The use of seismic stratigraphically defined thickness variations to constrain the timing of faulting comes with several uncertainties. First, it is worth noting that, although the observed thickness variations are sometimes small (10-20 m; see Fig. 5), they are above the seismic resolution, i.e. *the limit of separability* of ~10 m. Second, it may be argued that the observed thickening is strain related, merely being an artefact of complex fault interaction or differential compaction. However, based on the observation that: (1) thickness changes occur away from fault branchlines; and (2) the difference in burial between the hanging wall and footwall strata is relatively small due to the small fault throws, fault geometry-induced strain and differential compaction appear less likely to cause the observed across-fault thickness changes.

4.2 Fault analysis

To understand the kinematics of the polygonal fault system, we map 137 faults imaged in the selected area using strike-perpendicular seismic sections and coherency time slices (Bahorich and Farmer 1995). We extract the height and length, as well as the average strike and dip of these faults (Fig. 6). We also extract displacement-depth profiles and strike-projections to understand the kinematics of these faults (e.g. Walsh and Watterson 1989; Nicol et al. 1996). Displacement-depth profiles are extracted from each fault using strike-perpendicular seismic sections that intersect the high-displacement centres of the faults. To extract fault displacement, we: (1) correlate multiple seismic reflections across the fault plane; (2) identify the foot and hanging wall cut-offs of these reflections, i.e. the intersection points of the reflections and the fault; (3) measure the fault throw (*t*) and heave (*h*) as the vertical or horizontal distance between foot and hanging wall cut-offs, respectively; and (4) calculate the dip-parallel fault displacement (*d*) from the throw and have using Pythagoras' theorem (Figs. 7, 8):

$$d^2 = t^2 + h^2 \quad (1)$$

While the extraction does not include a strike-slip component, the polygonal faults studied here show no independent evidence of strike-slip displacement either (e.g. lateral offset of pre-kinematic depositional systems). Displacement-projections are extracted from four randomly-selected faults using strike-perpendicular seismic sections (Figs. 9, S2). Finally, we map the geometry these faults in dip section (Fig. 10) and cross-plot the extracted geometric data, such as fault height and dip (Fig. 11).

4.3 Strain estimation

To understand strain variability in polygonal fault systems, we use line and area measurements to estimate the layer-parallel strain at various structural levels in this system. The linear strain (ε_r) describes the change in length ($\Delta r = r_0 - r_1$) relative to the initial length (r_0) of a previously unstrained marker:

$$\epsilon_r = \frac{\Delta r}{r_0} \quad (2)$$

We approximate the initial length by the length of the section under consideration. The change in length is calculated as the sum of the fault heaves. The bed segments and fault heaves are extracted from 5.4 km long seismic sections located within the sub-volume, in four orientations and at multiple depths (Fig. 12). Because seismic sections oblique to normal faults may overestimate the measured strain, we also calculate strains from stratigraphic horizons. The areal strain of a surface describes the change in area ($\Delta A = A_0 - A_1$) relative to an initial area (A_0) of a previously unstrained marker:

$$\epsilon_A = \frac{\Delta A}{A_0} \quad (3)$$

To estimate this strain, we approximate the initial area (A_0) by the extent of the map and the final area (A_1) by the extent of the horizon without faults (Tab. 1). To allow a comparison to previous studies, we also convert areal to linear strains, assuming horizontal isotropy (Tab. 1), by relating area and length:

$$A = \pi r^2 \quad (4)$$

While these techniques capture visible deformation, it is worth noting that these estimates do not include sub-seismic deformation. Previous studies of tectonic faults, for instance, suggest that sub-seismic faults accommodate 25-60% of the total strain (Marrett and Allmendinger 1992). While previous studies suggest that polygonal faults can have displacements below the seismic resolution of this study contributing small amounts of strain (Henriet et al. 1988; Henriet et al. 1991), it is possible that the above calculation underestimates the layer-parallel strain in the system (see discussion). Finally, it is worth noting that, since these estimates are based on 3-D surfaces (rather than 2-D maps), the effect of folding is explicitly considered in our strain estimates. Folding a 3-D surface with constant area can result in an apparent area reduction when comparing 2-D maps before and after folding. This apparent area reduction would contribute to lateral strain estimates. To remove this artificial effect, we use 3-D surfaces (rather than 2-D maps) to estimate areal strains. Contractive strains are positive in our notation.

5. RESULTS

5.1 Fault geometries

The Hordaland Group-hosted fault system displays the characteristic polygonal pattern, including numerous fault segments linked in plan-view (Lonergan et al. 1998). The faults displace the opal-A/CT reflection, with fault heights varying between 100-800 m and lengths

238 from 100 to 3300 m (Fig. 2 and 10). The faults strikes show no dominant direction (Figs.
239 2,4,11). We identify a single tier that tips out upward and downwards onto the top Balder and
240 mid-Miocene unconformity reflections, respectively. Fault geometries ranging from planar to
241 listric in cross-section (Fig. 10). The planar faults have average dips of *c.* 20-50° (Fig. 10a),
242 whilst the dips of the listric faults decrease from *c.* 50° to *c.* 20° with depth (Fig. 10b). Planar
243 faults are commonly antithetic to listric faults (e.g. Fig. 2d).

244

245 *5.2 Stratigraphic thickness variations*

246 We observe prominent across-fault thickening (by up to 80 m) in the lower Hordaland
247 Group (Fig. 5f-h) and more subtle across-fault thickening (10-30 m) in the middle (Fig. 5d, e)
248 and upper Hordaland Group (Fig. 5a,b). The percentage of faults showing across-fault
249 thickness changes varies from ~10% in the upper (Fig. 5b) to ~50% in the lower Hordaland
250 Group (Fig. 5g).The system also changes from isolated fault traces in the upper Hordaland
251 Group (Fig. 5a,b) to a densely connected network in the middle Hordaland Group (Fig. 5f)
252 back to isolated fault traces in the lower Hordaland Group (Fig. 5h).

253

254 *5.3 Fault displacement*

255 Overall, 36% (49 of 137) of the mapped faults have symmetric, cone-shaped, c-type (Fig.
256 8a-c) displacement profiles (cf. Muraoka and Kamata 1983), whereas 64% (88 out of 137)
257 display asymmetric, b-type profiles, with the bulk of displacement occurring below their mid-
258 point (Fig. 8d-f). Faults with b-type profiles show the highest displacements (up to 200 m) in
259 the lower Hordaland Group, i.e. strata that were likely undergoing the opal-A/CT
260 transformation (Wrona et al. 2017a) (Fig. 8f). Whereas fault heaves are relatively high (up to
261 200 m) (Fig. 8e), throws are only slightly higher (up to 50 m) in these strata than observed at

shallow depths (Fig. 8d). Strike-projections of fault displacement highlight that multiple displacement maxima occur on the fault surface, typically occurring at broadly similar structural depths (Fig. 9). These projections also show relatively low displacement gradients (<0.2) near the upper (compared to the lower) tips of the faults (>0.2), and predominantly inclined upper tip lines and displacement contours. We note a correlation between the style of displacement-depth profile and fault geometry, with the majority of planar and listric faults having c- and b-type profiles, respectively (Figs. 8, 9). We also note that faults with b-type displacement-depth profiles are longer (~800 m), taller (~200 m) and accommodate more displacement (~60 m) than those with c-type profiles (Fig. 11c, d).

5.4 Strain estimates

Linear layer-parallel strains calculated from seismic sections resemble the b-type displacement profiles in that they show an asymmetric depth-dependent increase from 0.01 to 0.18 (Fig. 12). This pattern is persistent, occurring irrespective of the orientation of the seismic sections used for measurement. Linear layer-parallel strains calculated from structural maps show the same pattern; an asymmetric depth-dependent increase from 0.02 to 0.19 (Tab. 1)

6. DISCUSSION

6.1 Fault nucleation sites

This section infers the sites of fault nucleation from displacement data of 137 polygonal faults in the system. Displacement data of normal faults provide insights into their nucleation (and growth), particularly where they nucleate (e.g. Barnett et al. 1987; Walsh et al. 2003; Baudon and Cartwright 2008; Jackson and Rotevatn 2013). Displacement distributions were

first used to study the growth of blind faults, i.e. faults that do not interact with the surface (Watterson 1986; Barnett et al. 1987). According to the ideal model for the growth of a blind fault, displacement decreases from a maximum at the centre of the fault to zero at the tip line of the fault. The model predicts fault growth by radial tip-line propagation without migration of the position of maximum displacement. For an ideal blind fault, the point of maximum displacement therefore coincides with the point of fault nucleation. Displacement maxima may, however, move away from the point of nucleation due to segment linkage (e.g. Peacock and Sanderson 1991; Cartwright et al. 1995), mechanical heterogeneity (e.g. Gross 1995; Wilkins and Gross 2002), and/or mechanical interactions with adjacent structures (e.g. Nicol et al. 1996; Maerten et al. 1999; Morgan et al. 2015).

Displacement data extracted from 3-D seismic reflection data have been used to study the kinematics of polygonal faulting. For example, Neagu et al. (2010) extracted throw-depth profiles for 40 faults in a polygonal fault system in the Vøring and Møre basins, offshore mid-Norway and showed that throw maxima, typically indicating fault nucleation sites, occur both above and below the opal-A/CT transformation. These measurements do not however include fault heaves, which means that they probably underestimate displacement in the lower, shallow-dipping part of these broadly listric faults where fault heaves contribute a significant component to the total displacement. As such, their conclusion that the displacement maxima (i.e. nucleation sites) are also above the opal-A/CT transformation may be somewhat uncertain. Davies and Ireland (2011) extract three displacement-depth profiles from a polygonal fault system in the Vøring Basin and argue that the observed increase in fault displacement above the opal-A/CT transformation shows that differential subsidence due to silica diagenesis occurred in the hanging wall of these faults, and that this drove upward fault propagation (Fig. 8a in Davies and Ireland 2011). However, Davies and Ireland (2011) do not document: (1) how displacement was measured; (2) how throw measurements in time were

converted into metres; and (3) whether these profiles are representative for the large number of faults in the system. Another study by Laurent et al. (2012) extracts throws for 30 faults in a polygonal fault system imaged in 3D seismic reflection data in the Vøring Basin using a sequential stratigraphy analysis (Pauget et al. 2009). The analysed faults are planar, suggesting that throw measurements are broadly representative of the overall displacement. Despite having a larger number of faults than Davies and Ireland (2011) and although they do not suffer from measurement issues related to a listric fault-dominated systems (Neagu et al., 2010), Laurent et al. (2012) do not use their throw measurements, which show maxima above and below the opal-A/CT transformation, to infer polygonal fault kinematics. To summarise, the application of displacement data to understand the kinematics of polygonal faulting has thus far been inconclusive.

In this study, we find that 64% (88 of 137) of the analysed faults have b-type displacement depth-profiles with displacement maxima located in the lower Hordaland Group, below the opal-A/CT transformation (Fig. 8). This suggests that faults nucleated at this structural level, an interpretation supported by our observation of growth strata indicating fault activity in the lower Hordaland Group (see Section 6.3).

6.2 Fault mechanics

We now discuss the mechanics of polygonal fault nucleation and growth. Fault nucleation is commonly explained by initial failure of the host strata, which can be predicted from the friction angle (φ) of the host strata and the effective horizontal and vertical stress. A friction angle of 17° for the lower Hordaland Group is determined by Wensaas et al. (1998) using triaxial testing of side-wall cores from exploration well 25/7-2 (Fig. 2a). While this friction angle describes the current consolidated state of the host strata, the angle was

probably lower during fault nucleation, which likely occurred during shallow burial of these sediments, based on the observation that the faults reached the seabed and controlled the accumulation of growth strata. For example, Moore and Lockner (2007) indicate that the angle of friction can be as low as 3.4° in water saturated smectitc clays, such as those characterising the Hordaland Group mudstones. While it is difficult to determine the exact angle of friction of these sediments prior to fault nucleation, we can discuss the mechanics underlying fault nucleation, which are independent of a particular angle of friction.

First, we calculate the effective vertical stress (σ'_v), which is the difference between the lithostatic vertical stress (σ_v) and the pore fluid pressure (p_f):

$$\sigma'_v = \sigma_v - p_f \quad (5)$$

with the lithostatic vertical stress (σ_v) being:

$$\sigma_v = g\,\rho_s\,z \quad (6)$$

where g is the gravitational acceleration (9.81 m s^{-2}), ρ_s is the average (bulk) density of the lower Hordaland Group (~2000 kg m-3; Wrona et al. 2017a) and z is the depth (0-1 km). The pore fluid pressure can be expressed as the sum of the hydrostatic (p_h) and excess pore fluid pressure (p_e):

$$p_f = p_h + p_e \quad (7)$$

with

$$p_h = g\,\rho_w\,z \quad (8)$$

where ρ_w is the salt water density (1146 kg m^{-3}) (Rider and Kennedy 2011). The effective horizontal stress (σ'_h) can now be calculated by:

$$\sigma'_h = K_0 \, \sigma'_v \quad (9)$$

where K_0 is the coefficient of earth pressure at rest. The coefficient of earth pressure at rest for normally consolidated clays that have not been pre-compressed or pre-sheared (Terzaghi 1996), such as the mudstones of the Hordaland Group (Wensaas et al. 1998), can be calculated from the friction angle using Jaky's (1948) equation:

$$K_0 \approx 1 - sin(\varphi) \quad (10)$$

Possible angles of friction of 3.4-17° translate into earth pressures at rest of 0.7-0.94, which are in line with reported values for normally consolidated clays (Mayne and Kulhawy 1982; Jones 1994; Craig 2013).

Under these conditions, the stresses follow the K_0-path leading to 1-D compaction without sediment failure and fault nucleation (Fig. 13a, b). However, it is clear that failure and faulting occurred in the Hordaland Group. An early mechanical explanation for failure focussed on pore fluid overpressure (Cartwright 1994a, b). This hypothesis has subsequently been challenged by Goulty (2002), who argued that pore fluid overpressure causes the differential stress to decrease as the Mohr circle moves to the left (Engelder and Fischer 1994; Miller 1995), therefore avoiding failure or causing failure to occur in the tensile regime. A second mechanical explanation for fault nucleation invokes a reduction of the horizontal stresses (Cartwright and Lonergan 1996). To induce sediment failure and fault nucleation, the horizontal stress would need to be reduced to at least:

$$\sigma'_h = K_a \, \sigma'_v \quad (11)$$

where K_a refers to the active earth pressure for non-cohesive sediments (Fig. 13d):

$$K_a = \frac{1 - sin(\varphi)}{1 + sin(\varphi)} \quad (12)$$

For cohesive sediments, the horizontal stress would need to be reduced to (Fig. 13c; Bell, 1915):

$$\sigma'_h = K_a\,\sigma'_v - 2c\sqrt{K_a} \tag{13}$$

Subsequent suggestions for causes of horizontal stress reduction include syneresis (Dewhurst et al. 1999) and diagenesis (Shin et al. 2008; Cartwright 2011). There are, however, open questions regarding the plausibility of these processes; e.g. can syneresis and/or diagenesis reduce the horizontal effective stress to the point of shear failure at shallow depths (i.e. <100 m), as required for the syneresis model, and at low transformation rates, as required for diagenetic model? In our opinion, additional experimental studies, specifically designed to quantify the horizontal stress reduction in sediments and sedimentary rocks during syneresis and diagenesis, are required to decide if these two processes truly offer plausible explanations for the nucleation of polygonal fault systems.

After discussing the mechanics of fault nucleation, we can examine the mechanism driving fault growth. In general, slip along polygonal faults has been explained by low coefficients of residual friction (Goulty 2001, 2002, 2008). Rock mechanics predicts slip when the shear stresses at the fault overcome the residual shear strength. Although residual shear strengths of the Hordaland Group mudstones have not been determined, measurements on the stratigraphically equivalent London Clay indicate low angles of residual friction ($\varphi_r \approx$ 9°; Bishop et al. 1971). Under these conditions, the following equation (Jaeger et al. 2009):

$$K' = \left(\sqrt{1 + \tan(\varphi_r)^2} - \tan(\varphi_r)\right)^2 \tag{14}$$

predicts that earth pressures of ($K' \approx 0.9$) would suffice for these faults to slip (Fig. 13e). As this values (0.9) lies within the range of possible values of earth pressures at rest ($K_0 \approx 0.7 - 0.94$), low coefficients of residual friction offer a plausible explanation for the growth of these fault. Moreover, it is possible to speculate whether polygonal fault growth is more

generally controlled by coefficients of friction. Or, to put it another way, do polygonal fault systems exclusively grow in sediments that show a significant reduction in coefficients of friction during deformation? Note that this hypothesis could be tested by measuring coefficients of residual friction for a significant number of stratigraphic successions hosting polygonal fault systems.

6.3 Timing of fault activity

This section infers the timing of fault activity using high-resolution stratigraphic thickness maps. Previous studies constrain the timing of polygonal faulting by observing growth strata in 2-D seismic sections (Cartwright 1994a, b; Cartwright and Lonergan 1996) and/or stratigraphic thickness maps (Watterson et al. 2000; Stuevold et al. 2003; Morgan et al. 2015). As thickness maps are more robust than 2-D sections, we use stratigraphic thickness maps to constrain the timing of polygonal faulting in the northern North Sea. In the Hordaland Group-hosted polygonal fault system, thickness changes are most pronounced in the lower Hordaland Group (Fig. 5f-h), indicating that the main period of syn-depositional faulting occurred in the Eocene to Early Oligocene. Minor thickness changes (10-30 m) in the overlying, middle (Fig. 5d, e) and upper Hordaland Group (Fig. 5a,b) may result from continued activity until the late Oligocene-to-Miocene, or displacement decreases towards the upper fault tips.

6.4 Fault growth

After nucleation, normal faults grow in size and displacement, with the former typically involving tip-line propagation and segment linkage. In this study, fault growth was examined using a series of displacement-depth profiles and strike-projections (Fig. 8, 11). The analysis

shows two types of displacement-depth profiles: 64% (88 of 137 faults) have asymmetric b-type profiles with the bulk displacement in their lower halves and 36% (49 of 137 faults) have symmetric, cone-shaped c-type profiles (Fig. 8). Because faults with c-type profiles are generally: (1) smaller than the ones with b-type profiles (Fig. 11b); (2) have planar as opposed to listric geometries; and (3) are antithetic fault with b-type profiles (e.g. Fig. 2d), we suggest that the small planar faults accommodate bending stresses generated during hanging wall rollover of the large listric faults. Hence, the primary faults in this system are probably the larger ones defined by b-type displacement-depth profiles.

As outlined in Section 6.2, slip along these faults can, to a first degree, be explained by low coefficients of residual friction (Goulty 2001, 2002, 2008). Second order displacement (i.e. cumulative slip) variations may however help us understand the growth of this system. The primary faults show b-type displacement-depth profiles with high values in the lower Hordaland Group (Fig. 8f). Since the lower Hordaland Group has undergone silica diagenesis, it may be argued that displacement accumulation was driven by opal-A/CT transformation (e.g. by repeated slip due to horizontal stress reductions during opal-A dissolution). Irrespective of the problems associated with this argument (see Section 6.2), it is also possible to explain high displacement values by continues slip along the fault segments that nucleated first, i.e. the ones that nucleated in the lower Hordaland Group. It is thus not necessary to invoke silica diagenesis as a driver of fault growth to explain the observed displacement profiles and fault kinematics.

6.5 Orientation

Clausen et al. (1999) suggest that, based on their recognition of a dominant NW-SE strike within a broadly polygonal array, faults within the Hordaland Group developed due to

westward-directed gravitational sliding influenced by a far-field tectonic stresses. In contrast, our analysis of fault strikes along a horizon close to the intra-Oligocene unconformity mapped by Clausen et al. (1999) reveals a more-or-less uniform distribution of fault strikes (Fig. 2b). This observation is confirmed by extracting fault orientations along eleven horizons (Fig. 4) and by 3-D mapping of 137 polygonal faults within the sub-volume (Fig. 11a). The NW-SE strike we observe along only the deepest horizon reflects the orientation of major tectonic faults, rather than the polygonal fault system (Fig. 4k). We therefore conclude that this polygonal fault system shows no dominant fault strike, suggesting gravitational sliding and far-field tectonics played no or an imperceptible role in the growth of this system.

6.6 Strain

Polygonal fault systems consist of large numbers of normal faults with variable strike orientations and displacements of up to 200 m (Fig. 8). Early studies have suggested that the layer-parallel displacement of these faults is accommodated by regional extension of the host succession (e.g. Higgs and McClay 1993; Clausen et al. 1999); a hypothesis further developed by recent field studies suggesting polygonal faults form due to radial extension (Antonellini and Mollema 2015; Petracchini et al. 2015). As outlined above, it is difficult to explain the observed uniform distribution of fault strikes in this system by unidirectional gravity-driven or tectonic extension, but could radial extension of the host succession explain the observed fault displacement? Cartwright and Lonergan (1996) demonstrate that observed layer-parallel displacement on polygonal faults in the North Sea could be explained by: (1) external extension or (2) internal contraction of the host strata. External extension of these layer-bound fault systems requires strains of approximately 0.06 to 0.19 (Cartwright and Lonergan, 1996), which would need to be accommodated by compression or extrusion of host strata on the basin margins. Since there is still no evidence for either of these processes in the North Sea,

we conclude that the argument of Cartwright and Lonergan (1996) relating the observed layer-parallel fault displacement primarily to internal contraction of the host strata, is still valid.

To estimate the contractive strain in the system, we apply zero lateral strain boundary conditions to the host succession (*sensu* Cartwright and Lonergan 1996). Previous studies estimate layer-parallel strains of 0.06-0.19 (Cartwright and Lonergan 1996) and ~0.01 (Watterson et al. 2000) in polygonal fault systems. Using the same method as these studies, we measure linear layer-parallel strains of 0.01-0.18 (Fig. 12). Since seismic sections oblique to normal faults may overestimate these strains, we also calculate areal strains of eleven horizons and subsequently derive linear strains of 0.02-0.19, assuming horizontal isotropy (Fig. 4 and Tab. 1). Our estimates suggest that the Cenozoic polygonal fault system, we study here, accommodated layer-parallel strains of 0.01-0.19 depending on the depth of observation, which lies within the range of previously reported values for this system (Cartwright and Lonergan 1996).

At this point it is worth noting that, based on recent field studies, we may underestimate the total amount of strain in this system. A brief summary of field studies reveals that polygonal fault systems have been documented in: (1) Paleogene mudstones in Belgium (Henriet et al. 1988; Henriet et al. 1991; Verschuren 1992; Dehandschutter et al. 2004; Dehandschutter et al. 2005a; Dehandschutter et al. 2005b); (2) Cretaceous chalk in France and the UK (Hibsch et al. 2003); (3) Cretaceous chalk in Egypt (Tewksbury et al. 2014); (4) Jurassic sandstones in the US (Antonellini and Mollema 2015); and (5) Cretaceous to Paleogene carbonates, cherts, and marls in Italy (Petracchini et al. 2015). Whilst earlier studies examining polygonal fault systems in the field mapped faults as discrete slip surfaces (Henriet et al. 1988; Henriet et al. 1991; Verschuren 1992; Dehandschutter et al. 2004; Dehandschutter et al. 2005a; Dehandschutter et al. 2005b), recent work suggests that

491 ‘individual’ polygonal faults actually consist of dense clusters of slip surfaces (Tewksbury et
492 al. 2014; Antonellini and Mollema 2015; Petracchini et al. 2015). If the polygonal faults
493 mapped in this study consist of slip surfaces with displacements below the seismic resolution
494 (<10 m), we would underestimate the total strain in the system. Previous studies of tectonic
495 faults suggest that sub-seismic faults can accommodate 25-60% of the total strain (Marrett
496 and Allmendinger 1992). This highlights that layer-parallel contractive strains could as high
497 as 0.32 in the Hordaland Group system presented here.

498 Comparing layer-parallel strains with those resulting from conventional compaction is
499 important to understand the overall deformation of the succession hosting the polygonal fault
500 system. To estimate strains resulting from compaction, it is necessary to constrain on the
501 initial and current porosity of the host strata. While the current porosity of these strata is
502 ~0.35 (Wrona et al. 2017a; Wrona et al. 2017b), the initial porosity is poorly constrained.
503 Considering initial porosities of 0.45 to 0.85, the predicted volumetric strains vary between
504 0.22 and 0.59. This simple estimate highlights that this polygonal fault system accommodates
505 layer-parallel contractive strains (0.01-0.19) on the same order of magnitude as conventional
506 compaction (0.22-0.59).

507

508 **7. CONCLUSIONS**

509 We examine the kinematic evolution of polygonal faulting in the northern North Sea
510 using high-resolution 3-D seismic reflection and borehole data. Stratigraphic thickness
511 variations suggest the fault system initiated in the Eocene to Early Oligocene, and was likely
512 reactivated in the Late Oligocene to Middle Miocene. Displacement data indicate most (64%)
513 faults nucleated in the lower part of the host succession. The exact *trigger* for polygonal fault
514 system initiation remains elusive, although fault *growth* can be explained by low coefficients

of residual friction. In contrast, the wide range of fault strikes suggest basin-tilting and associated gravity-driven tectonics played no significant role in the initiation of this system, and that far-field tectonic stresses did not perturb the seemingly radially isotropic stress field. Strain estimates demonstrate that polygonal faulting resulted in significant layer-parallel contraction (strains: 0.01-0.19), approaching the same order of magnitude as conventional compaction.

ACKNOWLEDGEMENTS

We would like to thank the journal editor (Andrea Billi) and two anonymous reviewers for their extremely constructive and helpful comments, which significantly improved this manuscript. Moreover, we would like to thank the Department of Earth Science and Engineering, Imperial College for the Janet Watson scholarship that made this research possible. We thank Statoil and the Norwegian Petroleum Directorate for seismic and well data, and Schlumberger and Senergy for software licenses (Petrel, PetroMod and Interactive Petrophysics). We would like to thank Richard Jardine for explanations on the basic mechanics of sediment failure, Jens Jahren, Cedric John, Christian Berndt and Neil Goulty for helpful comments on previous versions of the manuscript, as well as Matthew Reeve, Johan Claringbould, Matthew Andrews and Sebastian Wolf for insightful discussions on the subject.

FIGURES

Fig. 1: Schematic diagram of a polygonal fault system comprised of a large numbers of layer-bound, low-displacement (<100 m throw) normal faults, which have a more-or-less polygonal arrangement in plan-view.

Fig. 2: a) Simplified structural map of the North Viking Graben, North Sea, highlighting major faults; the Horda, East Shetland Platform and Utsira High (after Holgate et al. 2013) and the outline of the 3-D seismic survey (b) in red; b) Outline of 3-D seismic survey (MN9201_R05) with coherency attribute map of seismic reflection of the opal-A/CT transformation in the Hordaland Group showing the characteristic polygonal fault pattern with more-or-less uniform distribution of fault strikes; the outline of the sub-cube (c), the location of exploration well 31/2-8 and the position of the key seismic section (d) are also indicated; c) coherency attribute map of sub-crop showing the position of polygonal faults used for detailed displacement extraction (Fig. 12); d) Arbitrary, fault-perpendicular seismic section showing listric polygonal faults that are confined to the Hordaland Group in the North Viking Graben.

Fig. 3: 3-D visualisation of depth-converted seismic sub-volume used for comprehensive seismic interpretation of eleven stratigraphic horizons (red dotted lines) within the interval hosting the studied polygonal fault system.

Fig. 4: Structural maps of stratigraphic horizons (a-k) showing the polygonal fault systems at different depth levels. Length-weighted rose diagrams extracted with NetworkGT (Nyberg et al. In Review), show a more-or-less uniform distribution of fault strikes (a-i).

Fig. 5: Thickness maps between stratigraphic horizons (Fig. 4) with example seismic sections (X-Y). On these maps, hanging wall wedges appear as gradual colour changes towards the fault (a, b, e), while across fault thickening appears as discrete colour jumps across faults (d-

j). These changes are also shown on representative strike-perpendicular seismic sections, inserted in the top right corner of these maps. Note that map c) contains no fault-related thickness changes and therefore is no accompanied by a seismic section.

Fig. 6: 3-D diagram of displacement distribution on normal fault illustrating the key fault properties (average strike, -dip, maximum length and -height) that were measured.

Fig. 7: Example of a planar polygonal fault (a) with c-type displacement-depth profile (b) in comparison with an example of a listric polygonal fault (c) with b-type displacement-depth profile (d).

Fig. 8: Throw-, heave- and displacement-depth profile of c-type (a-c) and b-type faults (d-f). Note the bulk displacement accumulated in the lower Hordaland Group.

Fig. 9: Displacement-strike-projection of four polygonal faults (a-d). Note that: (1) the bulk displacement has been accumulated in the lower Hordaland Group; (2) these faults show multiple displacement maxima at similar depth levels and (3) that they have low displacement gradients (<1) at the top. Branch lines are shown as dotted lines.

Fig. 10: a) Planar (i.e. constant dip) geometries of faults with c-type displacement-depth profiles and b) listric (i.e. downward decreasing dip) geometries of faults with b-type displacement-depth profiles in strike-perpendicular cross-section.

Fig. 11: Cross-plots of a) average strike and dip, b) maximum length and height, c), maximum height and displacement, and d) maximum length and displacement for 137 polygonal faults with b-type and c-type displacement depth profiles (Fig. 3). Note that these faults show no preferred orientation (a) and that b-type faults are longer, higher and accommodate more displacement than c-type faults (b-d).

Fig. 12: Seismic sections with lateral strain discretised onto polygonal faults. Strain was extracted from seismic sections in four directions (a-d). Note that the bulk strain has been accumulated in the lower Hordaland Group. See Figure 2b for location of sections.

Fig. 13: a) Mohr circles of effective stresses for burial under earth pressure at rest (K_0) relative to Coulomb failure envelope based on current mechanical properties of the lower Hordaland Group (Wensaas et al. 1998); b) Mohr circles of effective stresses for burial under earth pressure at rest (K_0) relative to Coulomb failure envelope based on mechanical properties of 'weak' clays (Moore and Lockner 2007), as expected during shallow burial; c) Mohr circles of effective stresses for burial for active earth pressure (K_a) relative to Coulomb failure envelope with cohesion and friction angle of the lower Hordaland Group (Wensaas et al. 1998); d) Mohr circles of effective stresses for burial for active earth pressure (K_a) relative to Coulomb failure envelope based on mechanical properties of 'weak' clays (Moore and Lockner 2007), as expected during shallow burial; e) Mohr circles of effective stresses for burial for earth pressure (K') relative to Coulomb failure envelope for low coefficients of residual friction ($\varphi_r \approx 9°$; Bishop et al. 1971).

TABLES

Horizon	A_0 [km²]	A_1 [km²]	ΔA [km²]	ε_A	r_0 [km]	r_1 [km]	Δr [km]	ε_r
a	46,61	44,82	1,78	0,04	3,85	3,78	0,13	0,02
b	46,61	42,83	3,78	0,08	3,85	3,69	0,28	0,04
c	46,61	39,58	7,03	0,15	3,85	3,55	0,54	0,08
d	46,61	36,89	9,71	0,21	3,85	3,43	0,75	0,11
e	46,61	36,91	9,69	0,21	3,85	3,43	0,75	0,11
f	46,61	36,92	9,69	0,21	3,85	3,43	0,75	0,11
g	46,61	30,72	15,88	0,34	3,85	3,13	1,28	0,19
h	46,61	33,55	13,05	0,28	3,85	3,27	1,03	0,15
i	46,61	32,59	14,01	0,30	3,85	3,22	1,12	0,16
j	46,61	30,66	15,95	0,34	3,85	3,12	1,29	0,19
k	46,61	39,90	6,71	0,14	3,85	3,56	0,51	0,07

Tab. 1: Area measurements and strain calculation for horizons shown on Fig. 4.

SUPPLEMENTARY FIGURE

Fig. S1: Plot showing check-shot data of exploration well 31/2-8 (orange) and linear velocity-depth functions (black), derived to convert seismic sub-cube from time to depth domain. Location of exploration well 31/2-8 is displayed on Fig. 2b.

Fig. S2: Seismic sections with fault displacement data used for the generation of the strike projection shown on Figure 11c. The 24 seismic sections are shown in order from east to west according to the strike projection. Note that the sections are five times vertically exaggerated.

REFERENCES

Anell, I., Thybo, H. & Rasmussen, E. 2012. A synthesis of Cenozoic sedimentation in the North Sea. *Basin Research*, **24**, 154-179, doi: DOI 10.1111/j.1365-2117.2011.00517.x.

Antonellini, M. & Mollema, P.N. 2015. Polygonal deformation bands. *Journal of Structural Geology*, **81**, 45-58.

Arts, R., Eiken, O., Chadwick, A., Zweigel, P., van der Meer, B. & Kirby, G. 2004. Seismic monitoring at the Sleipner underground CO2 storage site (North Sea). *Geological Society, London, Special Publications*, **233**, 181-191.

Badley, M.E., Price, J.D., Rambech Dahl, C. & Agdestein, T. 1988. The structural evolution of the northern Viking Graben and its bearing upon extensional modes of basin formation. *Journal of the Geological Society*, **145**, 455-472, doi: 10.1144/gsjgs.145.3.0455.

Bahorich, M. & Farmer, S. 1995. 3-D seismic discontinuity for faults and stratigraphic features: The coherence cube. *The leading edge*, **14**, 1053-1058.

Barnett, J.A.M., Mortimer, J., Rippon, J.H., Walsh, J.J. & Watterson, J. 1987. Displacement Geometry in the Volume Containing a Single Normal-Fault. *Aapg Bulletin-American Association of Petroleum Geologists*, **71**, 925-937.

Baudon, C. & Cartwright, J. 2008. The kinematics of reactivation of normal faults using high resolution throw mapping. *Journal of Structural Geology*, **30**, 1072-1084, doi: DOI 10.1016/j.jsg.2008.04.008.

Bell, A.L. 1915. THE LATERAL PRESSURE AND RESISTANCE OF CLAY AND THE SUPPORTING POWER OF CLAY FOUNDATIONS. *Minutes of the Proceedings of the Institution of Civil Engineers*. Thomas Telford-ICE Virtual Library, 233-272.

Bell, R.E., Jackson, C.A.L., Whipp, P.S. & Clements, B. 2014. Strain migration during multiphase extension: Observations from the northern North Sea. *Tectonics*, **33**, 1936-1963.

Bishop, A.W., Green, G., Garga, V.K., Andresen, A. & Brown, J. 1971. A new ring shear apparatus and its application to the measurement of residual strength. *Geotechnique*, **21**, 273-328.

Brown, A.R. 2004. Interpretation of three-dimensional seismic data.

Cartwright, J. 2011. Diagenetically induced shear failure of fine-grained sediments and the development of polygonal fault systems. *Marine and Petroleum Geology*, **28**, 1593-1610, doi: DOI 10.1016/j.marpetgeo.2011.06.004.

Cartwright, J., Huuse, M. & Aplin, A. 2007. Seal bypass systems. *AAPG Bulletin*, **91**, 1141-1166.

Cartwright, J., James, D. & Bolton, A. 2003. The genesis of polygonal fault systems: a review. *Subsurface Sediment Mobilization*, **216**, 223-243, doi: Doi 10.1144/Gsl.Sp.2003.216.01.15.

Cartwright, J.A. 1994a. Episodic Basin-Wide Fluid Expulsion from Geopressured Shale Sequences in the North-Sea Basin. *Geology*, **22**, 447-450, doi: Doi 10.1130/0091-7613(1994)022<0447:Ebwfef>2.3.Co;2.

Cartwright, J.A. 1994b. Episodic Basin-Wide Hydrofracturing of Overpressured Early Cenozoic Mudrock Sequences in the North-Sea Basin. *Marine and Petroleum Geology*, **11**, 587-607, doi: Doi 10.1016/0264-8172(94)90070-1.

Cartwright, J.A. & Lonergan, L. 1996. Volumetric contraction during the compaction of mudrocks: A mechanism for the development of regional-scale polygonal fault systems. *Basin Research*, **8**, 183-193, doi: DOI 10.1046/j.1365-2117.1996.01536.x.

Cartwright, J.A., Trudgill, B.D. & Mansfield, C.S. 1995. Fault Growth by Segment Linkage - an Explanation for Scatter in Maximum Displacement and Trace Length Data from the Canyonlands Grabens of Se Utah. *Journal of Structural Geology*, **17**, 1319-1326, doi: Doi 10.1016/0191-8141(95)00033-A.

Childs, C., Nicol, A., Walsh, J.J. & Watterson, J. 2003. The growth and propagation of synsedimentary faults. *Journal of Structural Geology*, **25**, 633-648.

Clausen, J., Gabrielsen, R., Reksnes, P. & Nysaether, E. 1999. Development of intraformational (Oligocene–Miocene) faults in the northern North Sea: influence of remote stresses and doming of Fennoscandia. *Journal of Structural Geology*, **21**, 1457-1475.

Craig, R.F. 2013. Soil mechanics. Springer.

Davies, R., Ireland, M. & Cartwright, J. 2009. Differential compaction due to the irregular topology of a diagenetic reaction boundary: a new mechanism for the formation of polygonal faults. *Basin Research*, **21**, 354-359.

Davies, R.J. & Ireland, M.T. 2011. Initiation and propagation of polygonal fault arrays by thermally triggered volume reduction reactions in siliceous sediment. *Marine Geology*, **289**, 150-158, doi: DOI 10.1016/j.margeo.2011.05.005.

Dehandschutter, B., Gaviglio, P., Sizun, J.-P., Sintubin, M., Vandycke, S., Vandenberghe, N. & Wouters, L. 2005a. Volumetric matrix strain related to intraformational faulting in argillaceous sediments. *Journal of the Geological Society*, **162**, 801-813.

Dehandschutter, B., Vandycke, S., Sintubin, M., Vandenberghe, N., Gaviglio, P., Sizun, J.-P. & Wouters, L. 2004. Microfabric of fractured Boom Clay at depth: a case study of brittle–ductile transitional clay behaviour. *Applied Clay Science*, **26**, 389-401.

Dehandschutter, B., Vandycke, S., Sintubin, M., Vandenberghe, N. & Wouters, L. 2005b. Brittle fractures and ductile shear bands in argillaceous sediments: inferences from Oligocene Boom Clay (Belgium). *Journal of Structural Geology*, **27**, 1095-1112.

690 Dewhurst, D.N., Cartwright, J.A. & Lonergan, L. 1999. The development of polygonal fault
691 systems by syneresis of colloidal sediments. *Marine and Petroleum Geology*, **16**, 793-810,
692 doi: Doi 10.1016/S0264-8172(99)00035-5.

693 Eidvin, T. & Rundberg, Y. 2001. Late Cainozoic stratigraphy of the Tampen area (Snorre and
694 Visund fields) in the northern North Sea, with emphasis on the chronology of early Neogene
695 sands. *Norwegian Journal of Geology/Norsk Geologisk Forening*, **81**.

696 Engelder, T. & Fischer, M.P. 1994. Influence of poroelastic behavior on the magnitude of
697 minimum horizontal stress, Sh in overpressured parts of sedimentary basins. *Geology*, **22**,
698 949-952, doi: Doi 10.1130/0091-7613(1994)022<0949:Iopbot>2.3.Co;2.

699 Faerseth, R.B., Knudsen, B.E., Liljedahl, T., Midboe, P.S. & Soderstrom, B. 1997. Oblique
700 rifting and sequential faulting in the Jurassic development of the northern North Sea. *Journal*
701 *of Structural Geology*, **19**, 1285-1302, doi: 10.1016/s0191-8141(97)00045-x.

702 Faleide, J.I., Kyrkjebo, R., Kjennerud, T., Gabrielsen, R.H., Jordt, H., Fanavoll, S. & Bjerke,
703 M.D. 2002. Tectonic impact on sedimentary processes during Cenozoic evolution of the
704 northern North Sea and surrounding areas. *Geological Society, London, Special Publications*,
705 **196**, 235-269, doi: 10.1144/gsl.sp.2002.196.01.14.

706 Gay, A. & Berndt, C. 2007. Cessation/reactivation of polygonal faulting and effects on fluid
707 flow in the Vøring Basin, Norwegian Margin. *Journal of the Geological Society*, **164**, 129-
708 141.

709 Giba, M., Walsh, J. & Nicol, A. 2012. Segmentation and growth of an obliquely reactivated
710 normal fault. *Journal of Structural Geology*, **39**, 253-267.

711 Goulty, N. 2001. Polygonal fault networks in fine-grained sediments–an alternative to the
712 syneresis mechanism. *First Break*, **19**, 69-73.

713 Goulty, N. 2002. Mechanics of layer-bound polygonal faulting in fine-grained sediments.
714 *Journal of the Geological Society*, **159**, 239-246.

715 Goulty, N. 2008. Geomechanics of polygonal fault systems: a review. *Petroleum Geoscience*,
716 **14**, 389-397.

717 Graham, C., Armour, A., Bathurst, P., Evans, D. & Petroleumsforening, N. 2003. The
718 Millennium Atlas: Petroleum Geology of the Central and Northern North Sea. Geological
719 Society of London.

720 Gross, M.R. 1995. Fracture partitioning: Failure mode as a function of lithology in the
721 Monterey Formation of coastal California. *Geological Society of America Bulletin*, **107**, 779-
722 792, doi: Doi 10.1130/0016-7606(1995)107<0779:Fpfmaa>2.3.Co;2.

Henriet, J., De Batist, M., Van Vaerenbergh, W. & Verschuren, M. 1988. Seismic facies and clay tectonic features of the Ypresian clay in the southern North Sea. *Bulletin van de Belgische Vereniging voor Geologie*, **97**, 457-472.

Henriet, J., De Batist, M. & Verschuren, M. 1991. Early fracturing of Palaeogene clays, southernmost North Sea: relevance to mechanisms of primary hydrocarbon migration. *Generation, accumulation and production of Europe's hydrocarbons*, **1**, 217-227.

Hibsch, C., Cartwright, J., Hansen, D., Gaviglio, P., André, G., Cushing, M., Bracq, P., Juignet, P., Benoit, P. & Allouc, J. 2003. Normal faulting in chalk: tectonic stresses vs. compaction-related polygonal faulting. *Geological Society, London, Special Publications*, **216**, 291-308.

Higgs, W. & McClay, K. 1993. Analogue sandbox modelling of Miocene extensional faulting in the Outer Moray Firth. *Geological Society, London, Special Publications*, **71**, 141-162.

Holgate, N.E., Jackson, C.A.-L., Hampson, G.J. & Dreyer, T. 2013. Sedimentology and sequence stratigraphy of the Middle–Upper Jurassic Krossfjord and Fensfjord formations, Troll Field, northern North Sea. *Petroleum Geoscience*, **19**, 237-258, doi: 10.1144/petgeo2012-039.

Huuse, M., Jackson, C.A.L., Van Rensbergen, P., Davies, R.J., Flemings, P.B. & Dixon, R.J. 2010. Subsurface sediment remobilization and fluid flow in sedimentary basins: an overview. *Basin Research*, **22**, 342-360.

Jackson, C.A.-L., Carruthers, D.T., Mahlo, S.N. & Briggs, O. 2014. Can polygonal faults help locate deep-water reservoirs? *AAPG Bulletin*, **98**, 1717-1738.

Jackson, C.A.-L. & Rotevatn, A. 2013. 3D seismic analysis of the structure and evolution of a salt-influenced normal fault zone: A test of competing fault growth models. *Journal of Structural Geology*, **54**, 215-234.

Jaeger, J.C., Cook, N.G. & Zimmerman, R. 2009. Fundamentals of rock mechanics. John Wiley & Sons.

Jaky, J. 1948. Pressure in silos. *Proceedings of the 2nd international conference on soil mechanics and foundation engineering*, 103-107.

Jones, M. 1994. Mechanical principles of sediment deformation. *The geological deformation of sediments*. Springer, 37-71.

Jordt, H., Faleide, J.I., Bjørlykke, K. & Ibrahim, M.T. 1995. Cenozoic sequence stratigraphy of the central and northern North Sea Basin: tectonic development, sediment distribution and provenance areas. *Marine and Petroleum Geology*, **12**, 845-879.

Jordt, H., Thyberg, B.I. & Nottvedt, A. 2000. Cenozoic evolution of the central and northern North Sea with focus on differential vertical movements of the basin floor and surrounding

clastic source areas. *Geological Society, London, Special Publications*, **167**, 219-243, doi: 10.1144/gsl.sp.2000.167.01.09.

Joy, A.M. 1993. Comments on the pattern of post-rift subsidence in the Central and Northern North Sea Basin. *Geological Society, London, Special Publications*, **71**, 123-140, doi: 10.1144/gsl.sp.1993.071.01.06.

Knox, R.W.O.B. & Holloway, S. 1992. 1. Paleogene of the central and northern North Sea. British Geological Survey Nottingham.

Kyrkjebø, R., Kjennerud, T., Gillmore, G., Faleide, J. & Gabrielsen, R. 2001. Cretaceous-Tertiary palaeo-bathymetry in the northern North Sea; integration of palaeo-water depth estimates obtained by structural restoration and micropalaeontological analysis. *Norwegian Petroleum Society Special Publications*, **10**, 321-345.

Laurent, D., Gay, A., Baudon, C., Berndt, C., Soliva, R., Planke, S., Mourgues, R., Lacaze, S., Pauget, F. & Mangue, M. 2012. High-resolution architecture of a polygonal fault interval inferred from geomodel applied to 3D seismic data from the Gjallar Ridge, Vøring Basin, Offshore Norway. *Marine Geology*, **332**, 134-151.

Lonergan, L., Cartwright, J. & Jolly, R. 1998. The geometry of polygonal fault systems in Tertiary mudrocks of the North Sea. *Journal of Structural Geology*, **20**, 529-548, doi: Doi 10.1016/S0191-8141(97)00113-2.

Løseth, H., Raulline, B. & Nygård, A. 2013. Late Cenozoic geological evolution of the northern North Sea: development of a Miocene unconformity reshaped by large-scale Pleistocene sand intrusion. *Journal of the Geological Society*, **170**, 133-145.

Maerten, L., Willemse, E.J., Pollard, D.D. & Rawnsley, K. 1999. Slip distributions on intersecting normal faults. *Journal of Structural Geology*, **21**, 259-272.

Marrett, R. & Allmendinger, R.W. 1992. Amount of extension on" small" faults: An example from the Viking graben. *Geology*, **20**, 47-50.

Mayne, P.W. & Kulhawy, F.H. 1982. Ko- OCR Relationships in Soil. *Journal of the Soil Mechanics and Foundations Division*, **108**, 851-872.

McLeod, A.E., Dawers, N. & Underhill, J. 2000. The propagation and linkage of normal faults: insights from the Strathspey–Brent–Statfjord fault array, northern North Sea. *Basin Research*, **12**, 263-284.

Miller, T.W. 1995. New insights on natural hydraulic fractures induced by abnormally high pore pressures. *AAPG Bulletin*, **79**, 1005-1018.

Moore, D.E. & Lockner, D.A. 2007. Friction of the smectite clay montmorillonite. *The seismogenic zone of subduction thrust faults*, 317-345.

792 Morgan, D., Cartwright, J. & Imbert, P. 2015. Perturbation of polygonal fault propagation by
793 buried pockmarks and the implications for the development of polygonal fault systems.
794 *Marine and Petroleum Geology*, **65**, 157-171.

795 Muraoka, H. & Kamata, H. 1983. Displacement Distribution Along Minor Fault Traces.
796 *Journal of Structural Geology*, **5**, 483-495, doi: Doi 10.1016/0191-8141(83)90054-8.

797 Nadin, P. & Kusznir, N. 1995. Palaeocene uplift and Eocene subsidence in the northern North
798 Sea Basin from 2D forward and reverse stratigraphic modelling. *Journal of the Geological*
799 *Society*, **152**, 833-848.

800 Neagu, R.C., Cartwright, J. & Davies, R. 2010. Measurement of diagenetic compaction strain
801 from quantitative analysis of fault plane dip. *Journal of Structural Geology*, **32**, 641-655, doi:
802 DOI 10.1016/j.jsg.2010.03.010.

803 Nicol, A., Watterson, J., Walsh, J.J. & Childs, C. 1996. The shapes, major axis orientations
804 and displacement patterns of fault surfaces. *Journal of Structural Geology*, **18**, 235-248, doi:
805 Doi 10.1016/S0191-8141(96)80047-2.

806 Nyberg, B., Nixon, C.W. & Sanderson, D.J. In Review. NetworkGT: A GIS tool for
807 Geometric and Topological Analysis of two-dimensional Fracture Networks. *Geosphere*.

808 Pauget, F., Lacaze, S. & Valding, T. 2009. A global approach in seismic interpretation based
809 on cost function minimization. *2009 SEG Annual Meeting*. Society of Exploration
810 Geophysicists.

811 Peacock, D. & Sanderson, D. 1991. Displacements, segment linkage and relay ramps in
812 normal fault zones. *Journal of Structural Geology*, **13**, 721-733, doi: Doi 10.1016/0191-
813 8141(91)90033-F.

814 Petracchini, L., Antonellini, M., Billi, A. & Scrocca, D. 2015. Syn-thrusting polygonal normal
815 faults exposed in the hinge of the Cingoli anticline, northern Apennines, Italy. *Frontiers in*
816 *Earth Science*, **3**, 67.

817 Rider, M.H. & Kennedy, M. 2011. The geological interpretation of well logs.

818 Rundberg, Y. 1989. Tertiary Sedimentary History and Basin Evolution of the Norwegian
819 North Sea Between 60˚-62˚N: An Integrated Approach. Universititet i Trondheim, Norges
820 tekniske høgskole.

821 Rundberg, Y. & Eidvin, T. 2005. Controls on depositional history and architecture of the
822 Oligocene-Miocene succession, northern North Sea Basin. *In*: Bjørn T.G Wandås, J.P.N.E.E.
823 & Felix, G. (eds.) *Norwegian Petroleum Society Special Publications*. Elsevier, 207-239.

824 Shin, H., Santarnarina, J.C. & Cartwright, J.A. 2008. Contraction-driven shear failure in
825 compacting uncemented sediments. *Geology*, **36**, 931-934, doi: Doi 10.1130/G24951a.1.

826 Stuevold, L.M., Faerseth, R.B., Arnesen, L., Cartwright, J. & Möller, N. 2003. Polygonal
827 faults in the Ormen Lange field, Møre basin, offshore mid Norway. *Geological Society,*
828 *London, Special Publications*, **216**, 263-281.

829 Taylor, S.K., Bull, J.M., Lamarche, G. & Barnes, P.M. 2004. Normal fault growth and linkage
830 in the Whakatane Graben, New Zealand, during the last 1.3 Myr. *Journal of Geophysical*
831 *Research: Solid Earth*, **109**.

832 Terzaghi, K. 1996. Soil mechanics in engineering practice. John Wiley & Sons.

833 Tewksbury, B.J., Hogan, J.P., Kattenhorn, S.A., Mehrtens, C.J. & Tarabees, E.A. 2014.
834 Polygonal faults in chalk: Insights from extensive exposures of the Khoman Formation,
835 Western Desert, Egypt. *Geology*, **42**, 479-482, doi: 10.1130/g35362.1.

836 Verschuren, M. 1992. *An integrated 3D approach to clay tectonic deformation and the*
837 *development of a new 3D surface modelling method*.

838 Walsh, J.J., Bailey, W.R., Childs, C., Nicol, A. & Bonson, C.G. 2003. Formation of
839 segmented normal faults: a 3-D perspective. *Journal of Structural Geology*, **25**, 1251-1262,
840 doi: Pii S0191-8141(02)00161-X

841 Doi 10.1016/S0191-8141(02)00161-X.

842 Walsh, J.J. & Watterson, J. 1989. Displacement gradients on fault surfaces. *Journal of*
843 *Structural Geology*, **11**, 307-316, doi: Doi 10.1016/0191-8141(89)90070-9.

844 Watterson, J. 1986. Fault Dimensions, Displacements and Growth. *Pure and Applied*
845 *Geophysics*, **124**, 365-373, doi: Doi 10.1007/Bf00875732.

846 Watterson, J., Walsh, J., Nicol, A., Nell, P. & Bretan, P. 2000. Geometry and origin of a
847 polygonal fault system. *Journal of the Geological Society*, **157**, 151-162.

848 Wensaas, L., Aagaard, P., Berre, T. & Roaldset, E. 1998. Mechanical properties of North Sea
849 Tertiary mudrocks: investigations by triaxial testing of side-wall cores. *Clay Minerals*, **33**,
850 171-183.

851 Wilkins, S.J. & Gross, M.R. 2002. Normal fault growth in layered rocks at Split Mountain,
852 Utah: influence of mechanical stratigraphy on dip linkage, fault restriction and fault scaling.
853 *Journal of Structural Geology*, **24**, 1413-1429.

854 Wrona, T., Jackson, C.A.-L., Huuse, M. & Taylor, K.G. 2017a. Silica diagenesis in Cenozoic
855 mudstones of the North Viking Graben: physical properties and basin modelling. *Basin*
856 *Research.*

857 Wrona, T., Taylor, K.G., Jackson, C.A.L., Huuse, M., Najorka, J. & Pan, I. 2017b. Impact of
858 silica diagenesis on the porosity of fine-grained strata: An analysis of Cenozoic mudstones
859 from the North Sea. *Geochemistry, Geophysics, Geosystems*.

860 Yielding, G. 1990. Footwall Uplift Associated with Late Jurassic Normal Faulting in the
861 Northern North-Sea. *Journal of the Geological Society*, **147**, 219-222, doi: DOI
862 10.1144/gsjgs.147.2.0219.

863

Figure 1.TIF

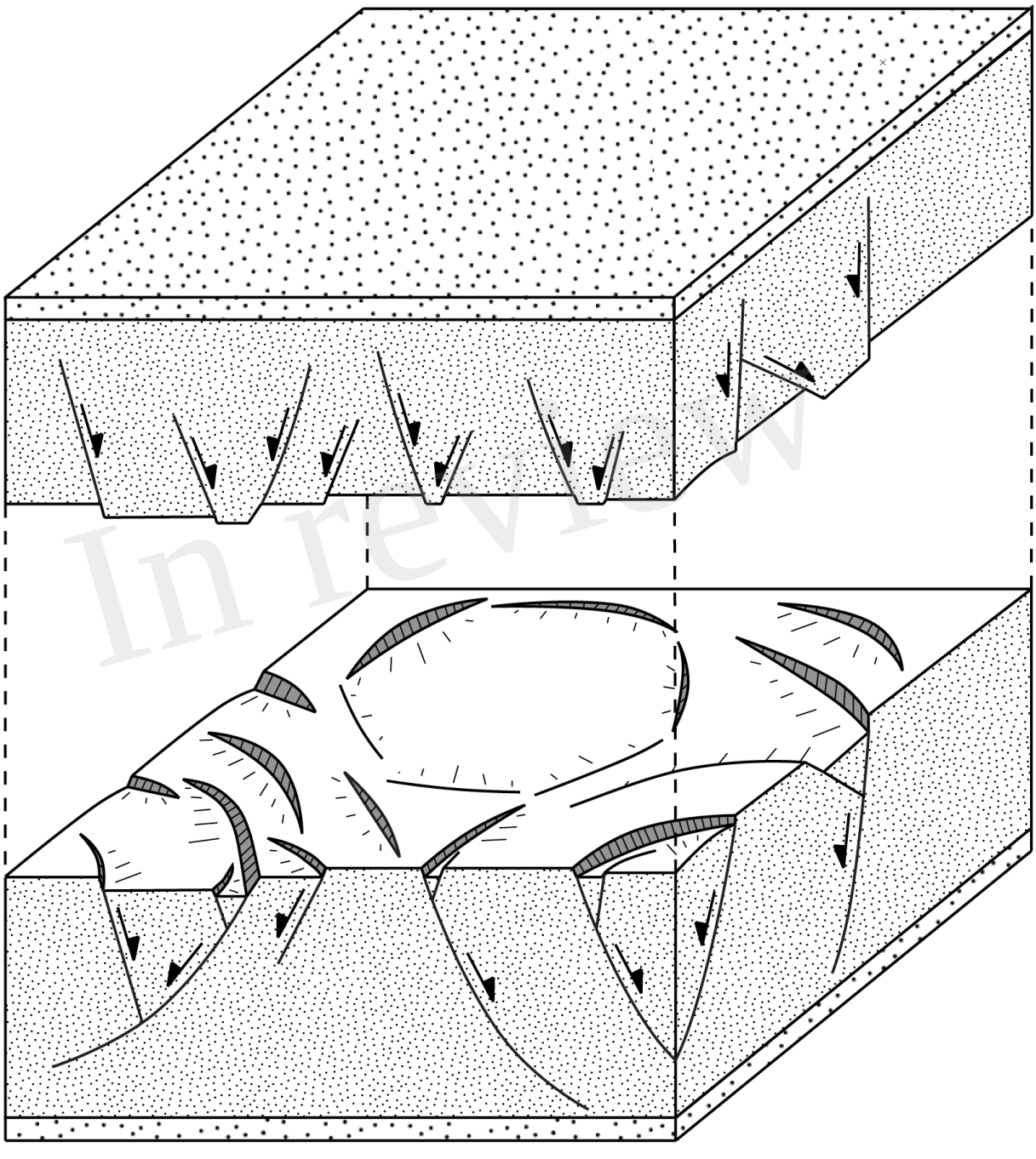

Fig. 1

Figure 2.TIF

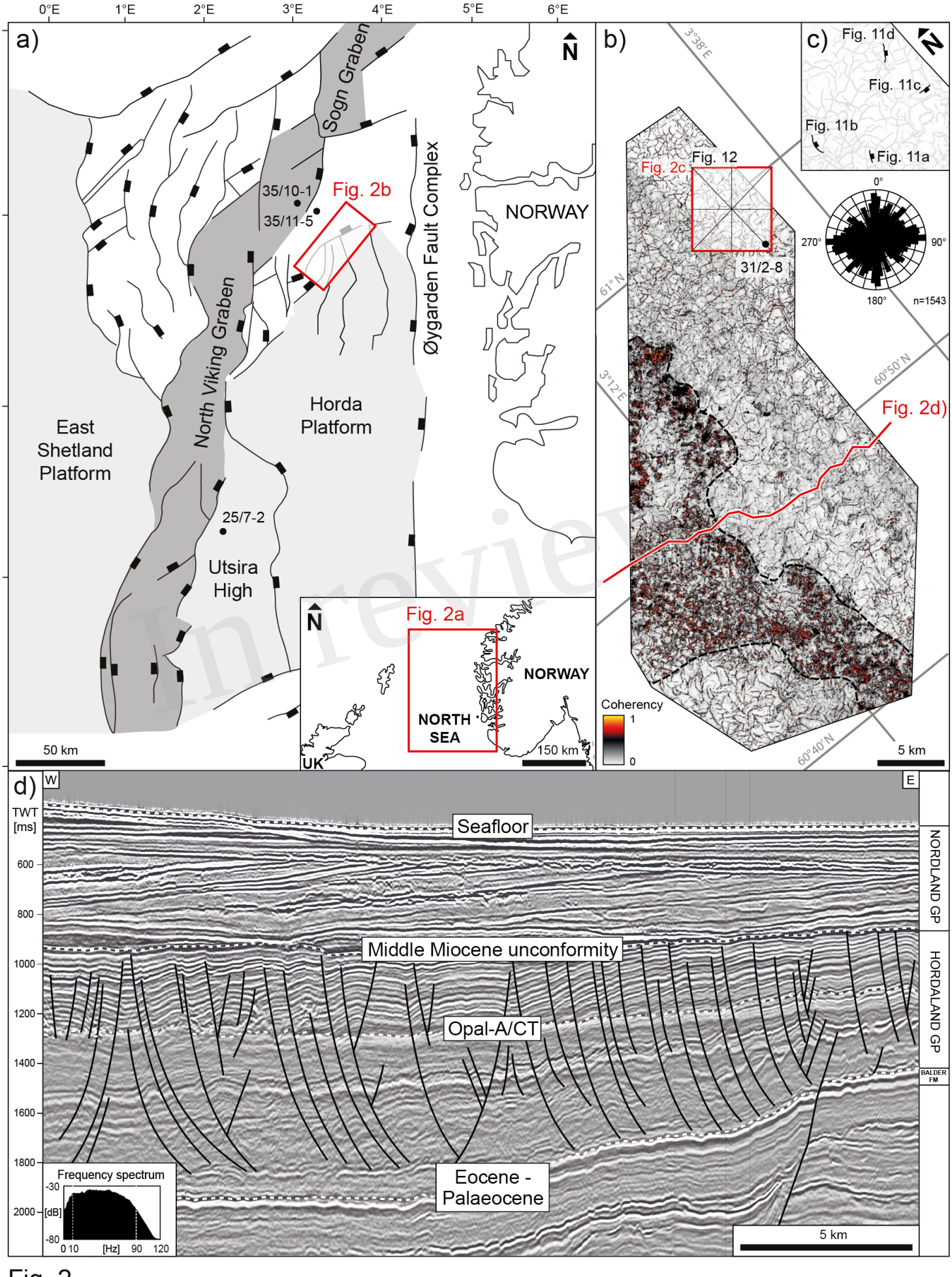

Fig. 2

Figure 3.TIF

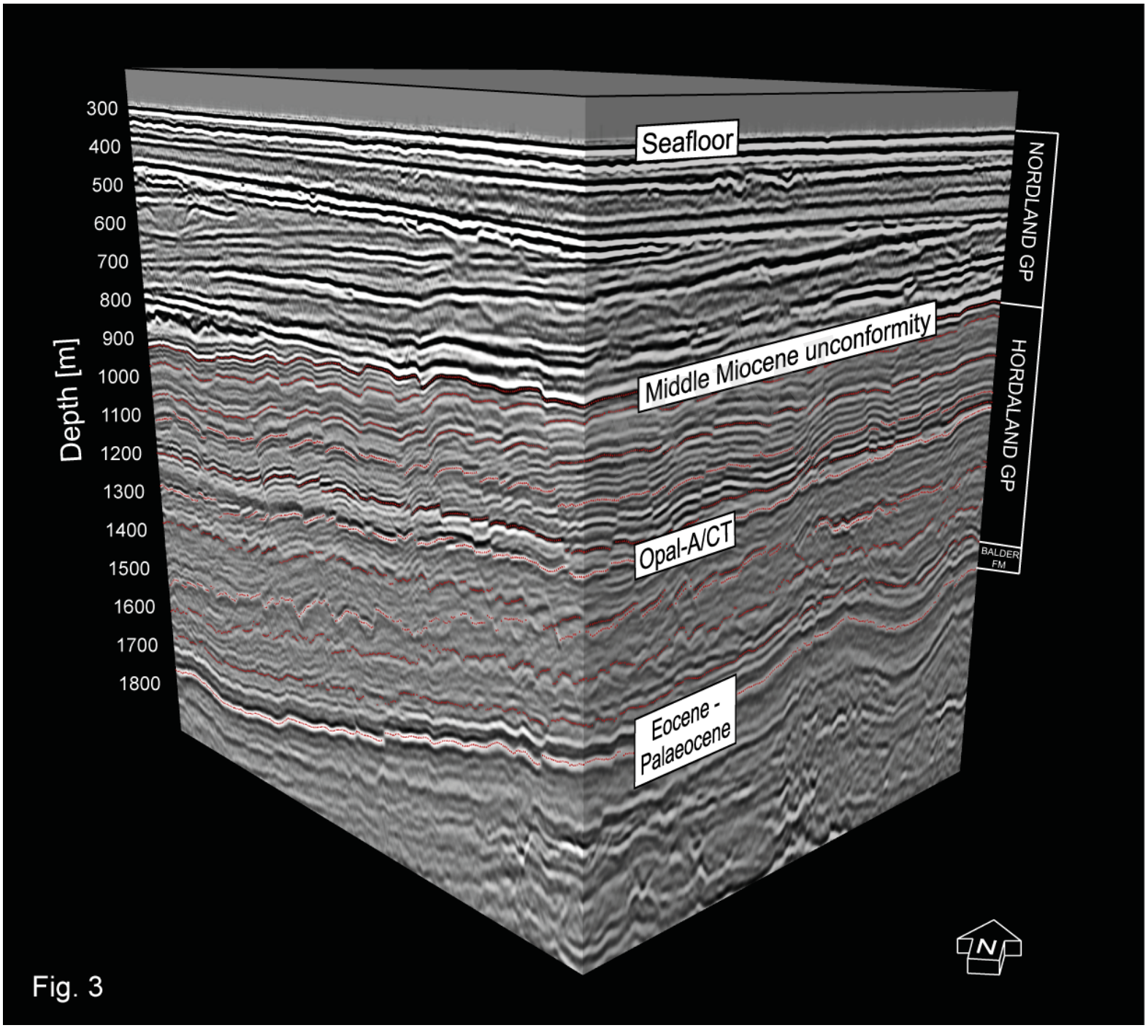

Fig. 3

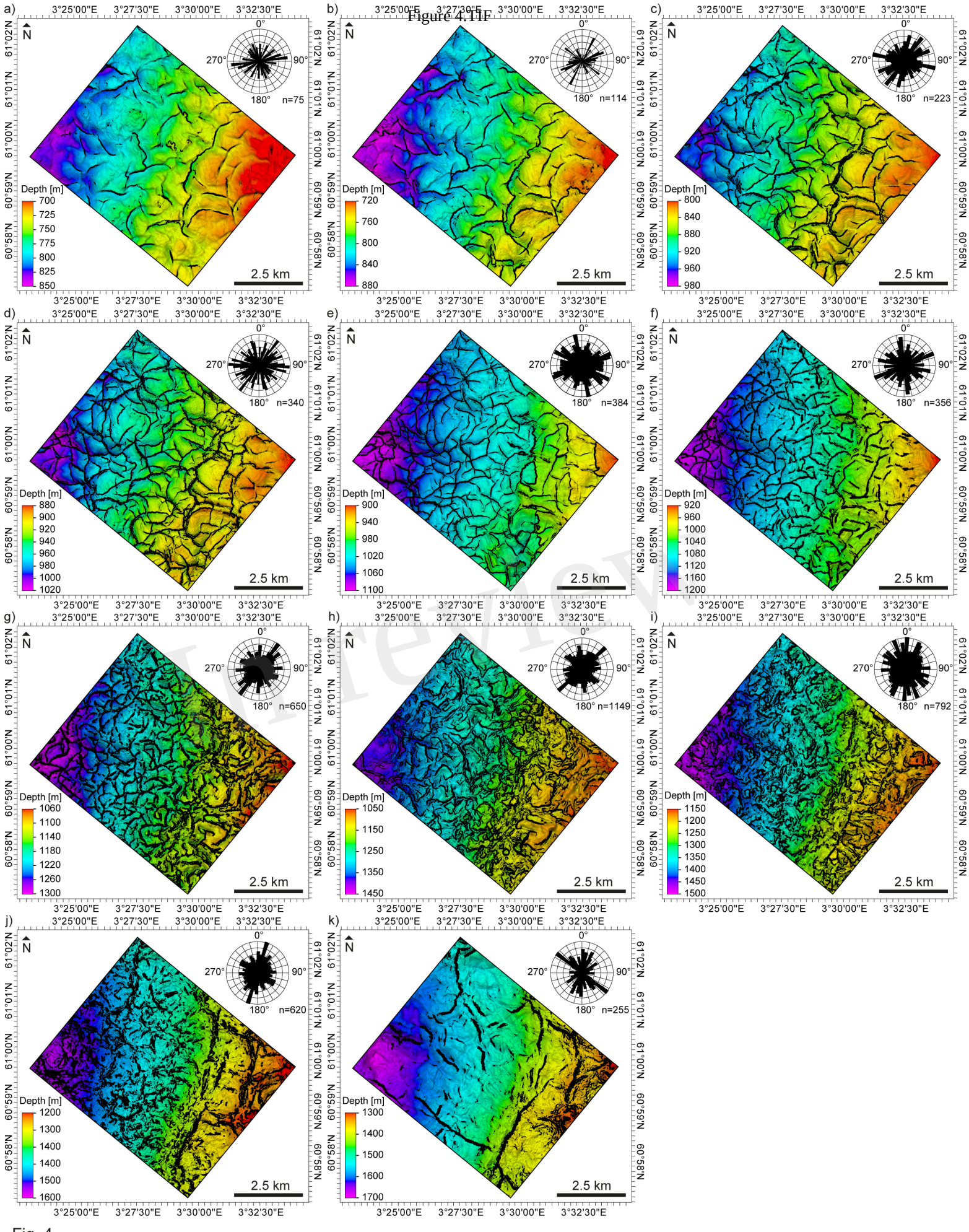
a)
b)
c)
d)
e)
f)
g)
h)
i)
j)
k)
N
0°
90°
180°
270°
n=75
n=114
n=223
n=340
n=384
n=356
n=650
n=1149
n=792
n=620
n=255
Depth [m]
700 725 750 775 800 825 850
720 760 800 840 880
800 840 880 920 960 980
880 900 920 940 960 980 1000 1020
900 940 980 1020 1060 1100
920 960 1000 1040 1080 1120 1160 1200
1060 1100 1140 1180 1220 1260 1300
1050 1150 1250 1350 1450
1150 1200 1250 1300 1350 1400 1450 1500
1200 1300 1400 1400 1500 1600
1300 1400 1500 1600 1700
2.5 km
3°25'00"E
3°27'30"E
3°30'00"E
3°32'30"E
61°02'N
61°01'N
61°00'N
60°59'N
60°58'N

Fig. 4

Figure 5.TIF

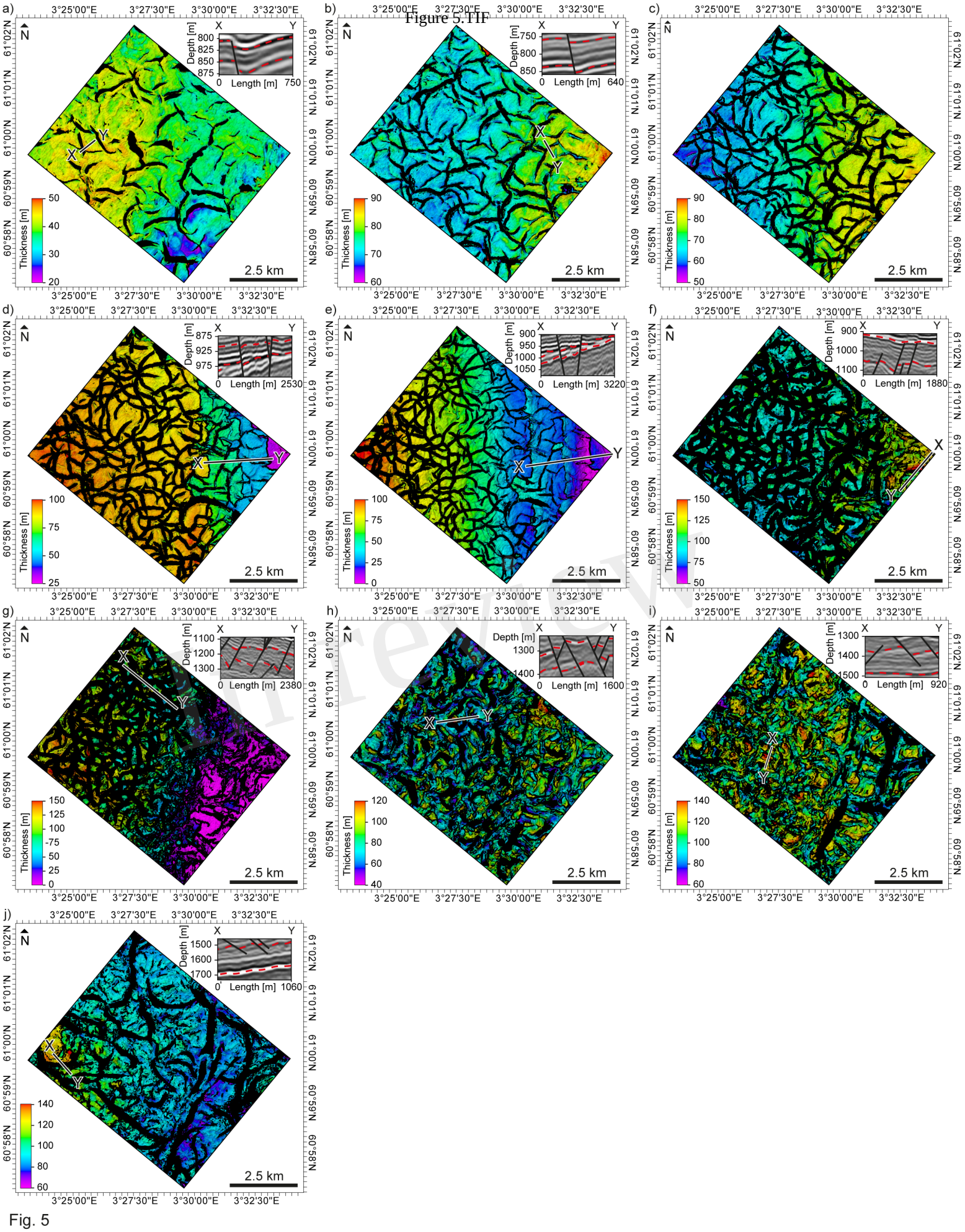

Fig. 5

Figure 6.TIF

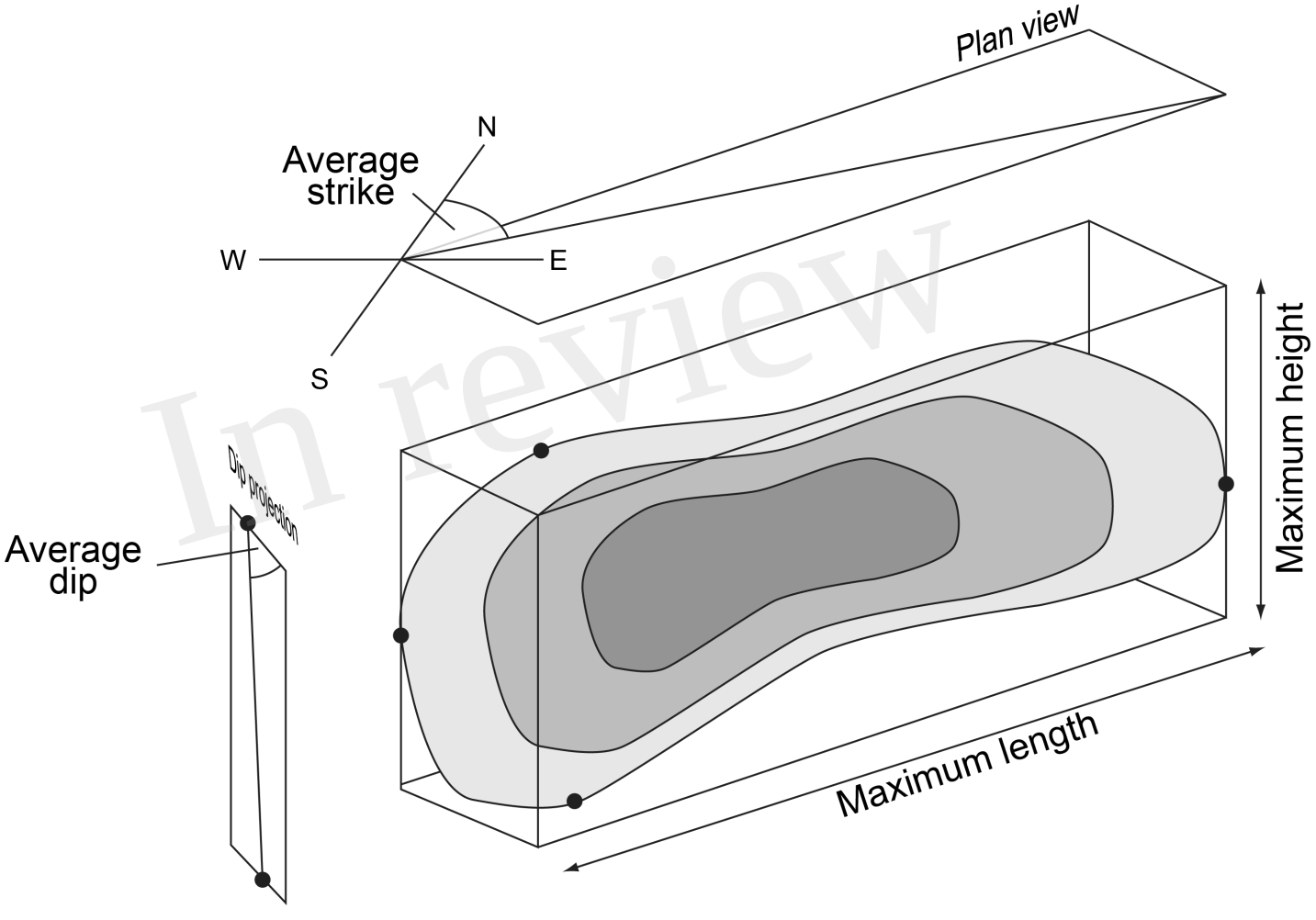

Fig. 6

Figure 7.TIF

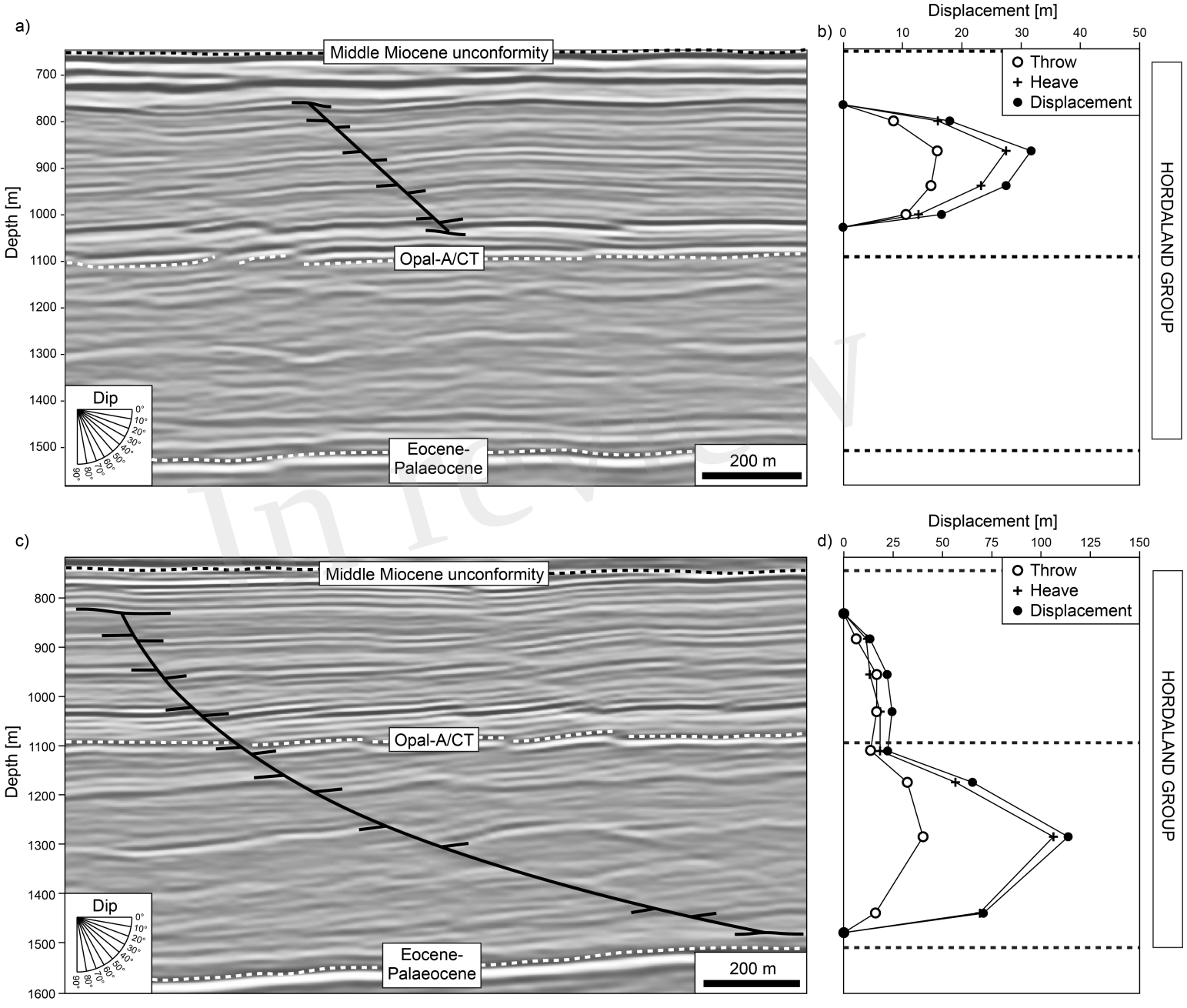

Fig. 7

Figure 8.TIF

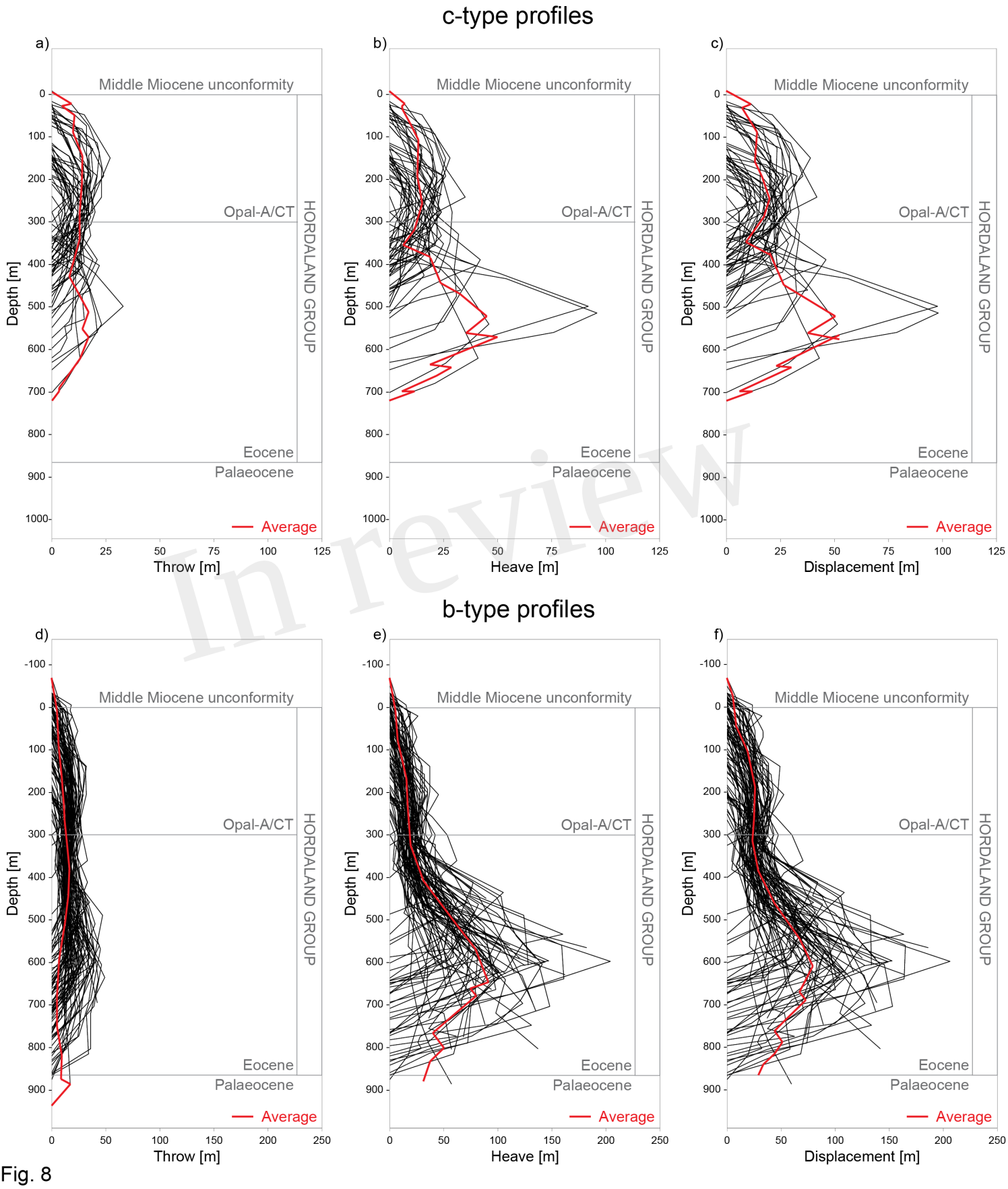

Fig. 8

Figure 9.TIF

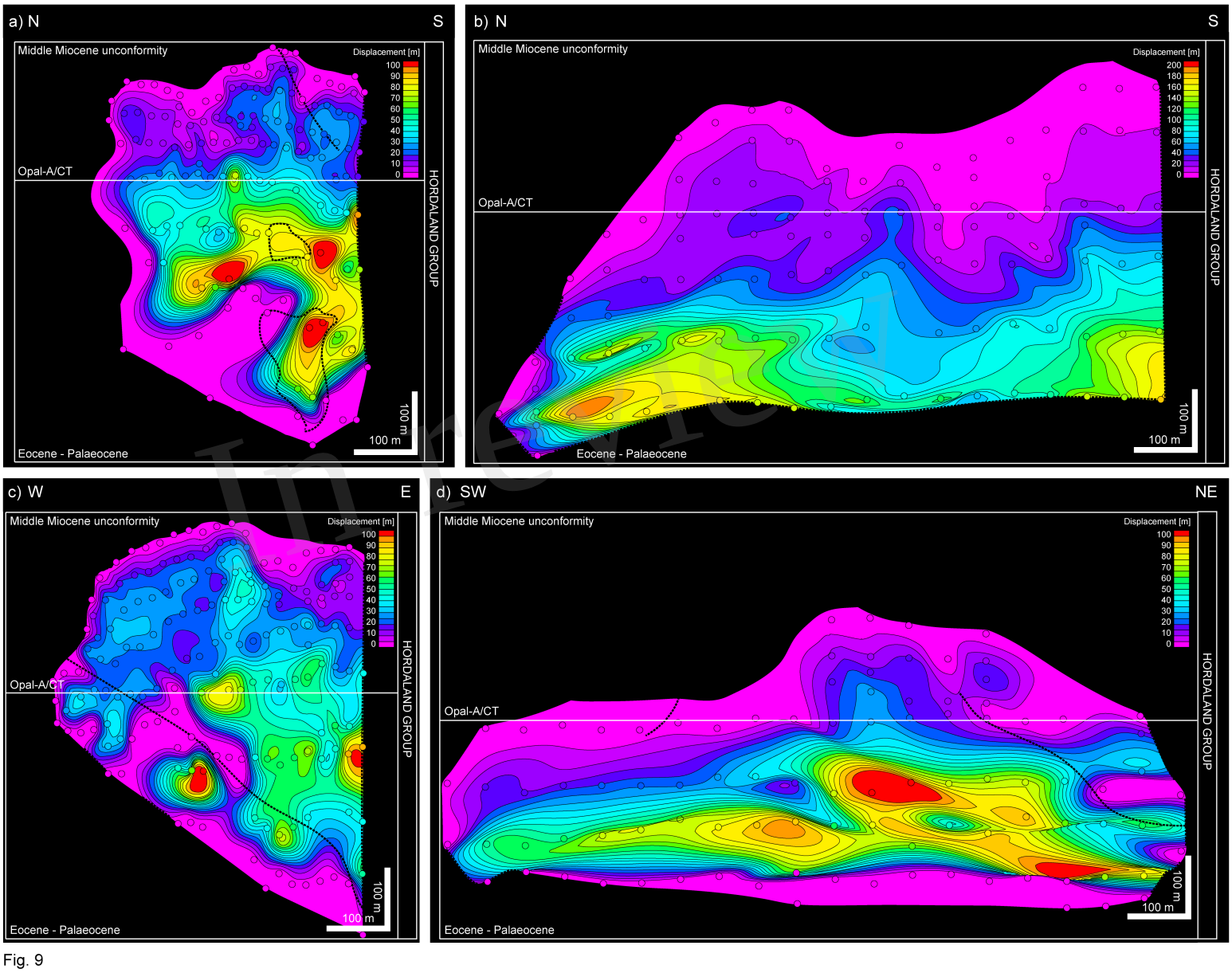

Fig. 9

Figure 10.TIF

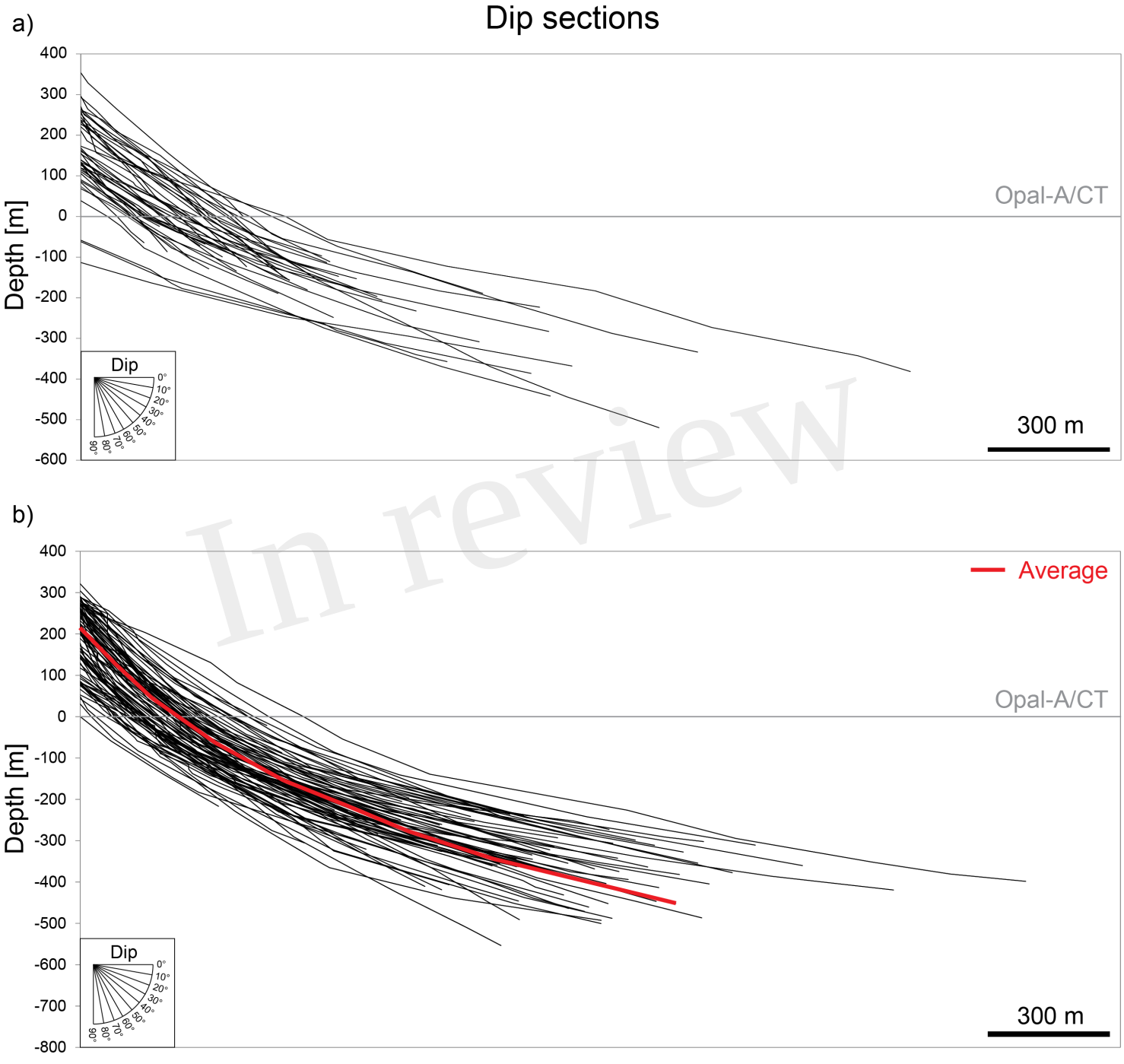

Fig. 10

Figure 11.TIF

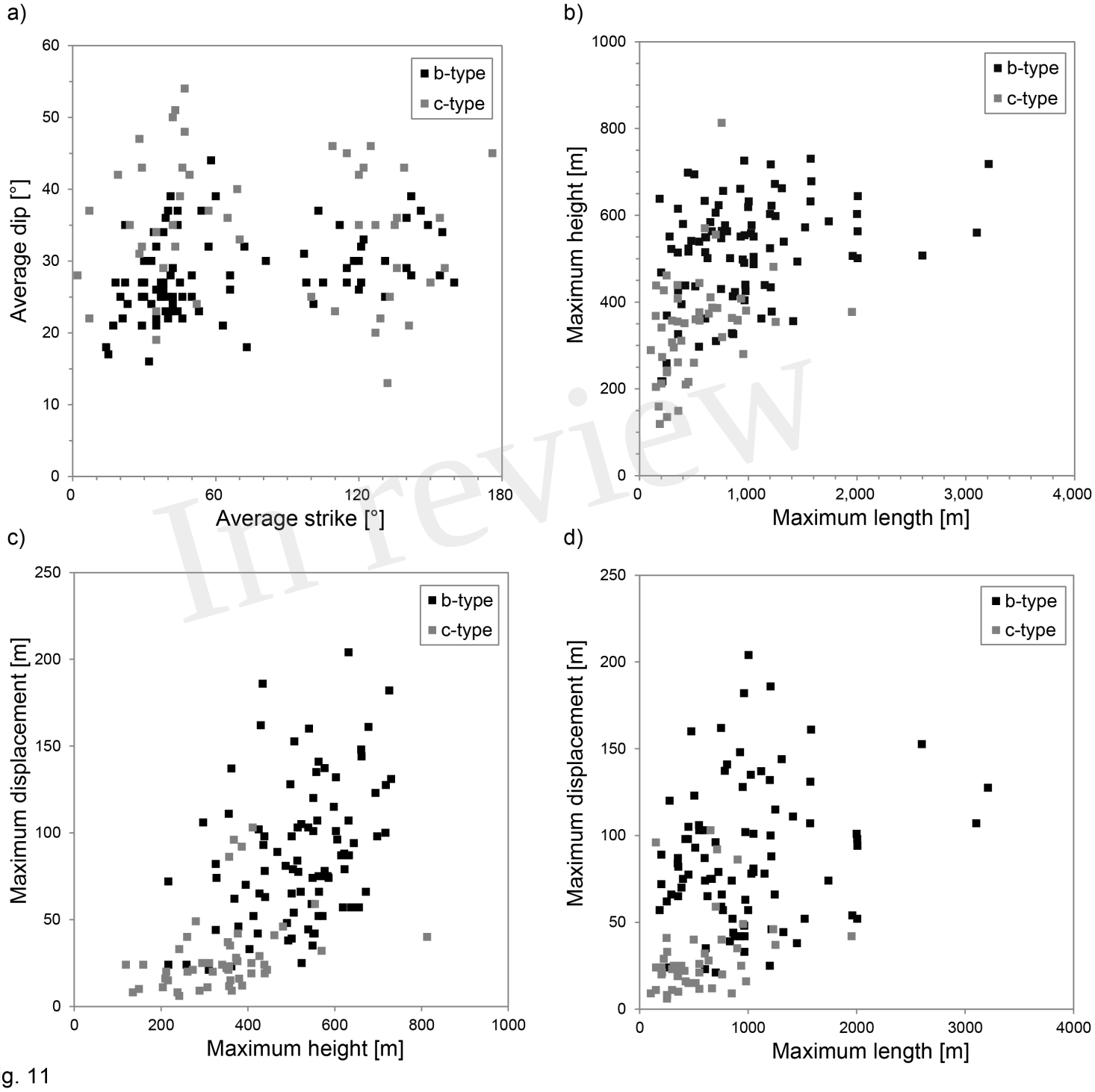

Fig. 11

Figure 12.TIF

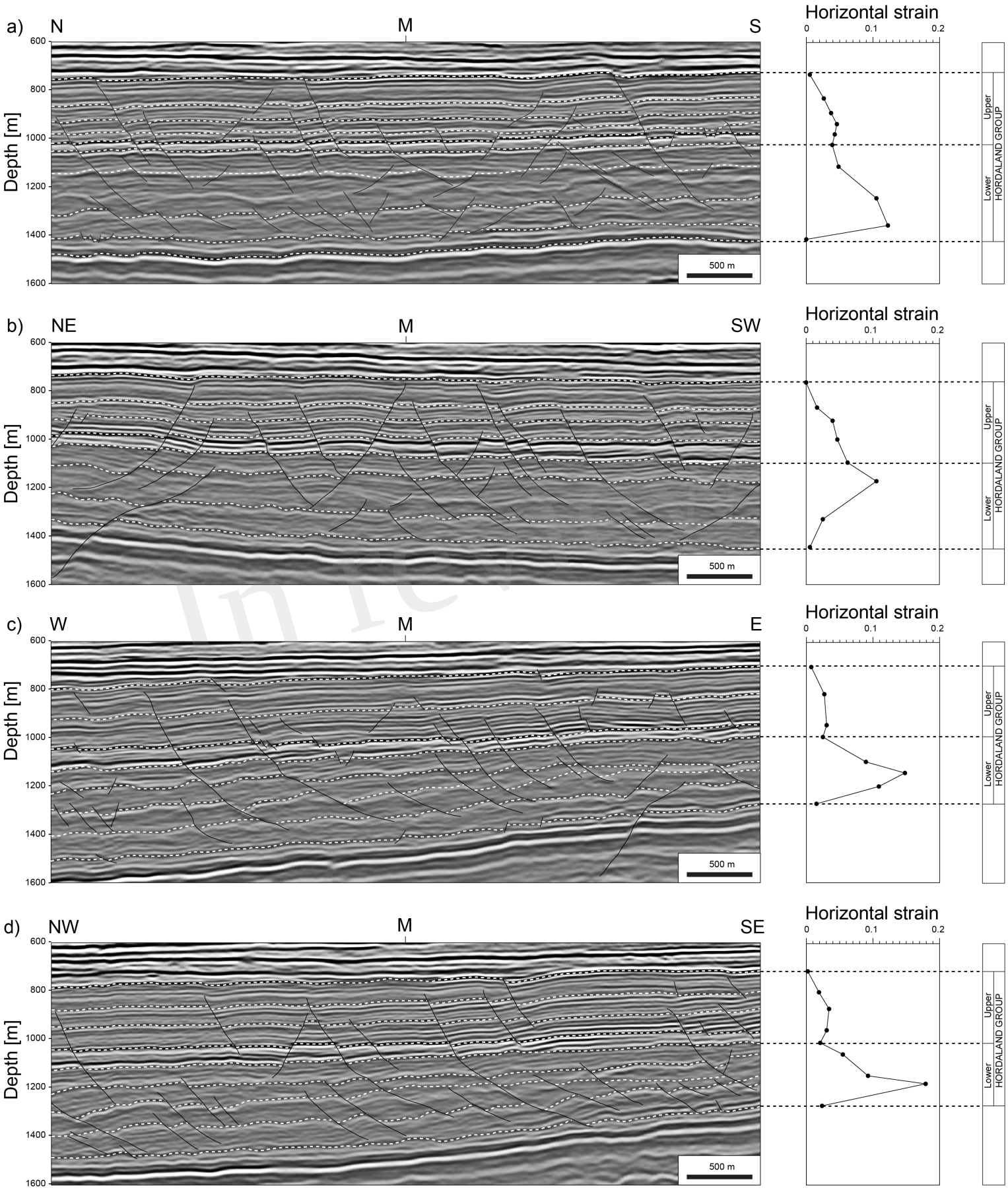

Fig. 12

Figure 13.TIF

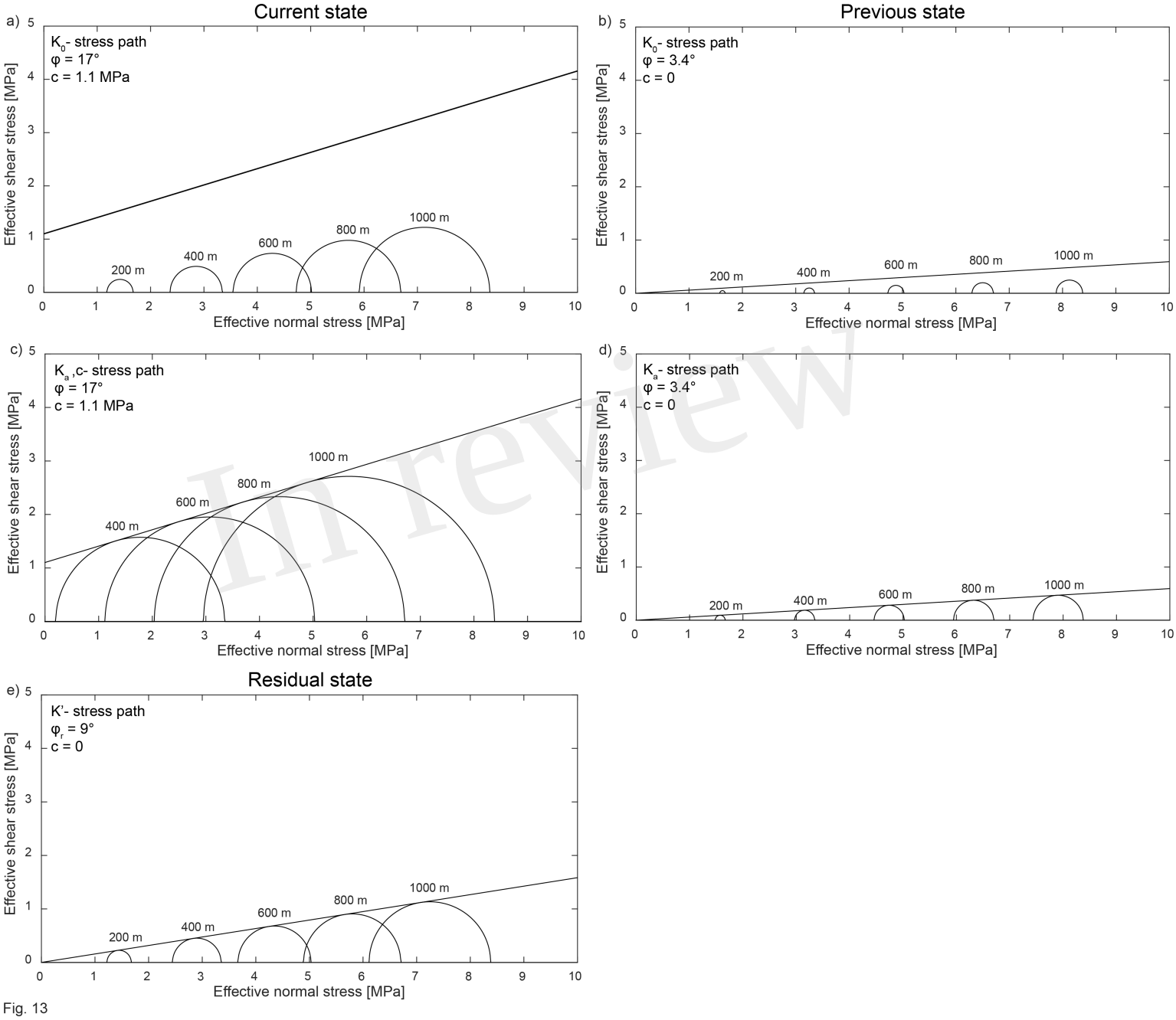

Fig. 13